Marine Geology 464 (2023) 107144

Contents lists available at ScienceDirect

Marine Geology

journal homepage: www.elsevier.com/locate/margo

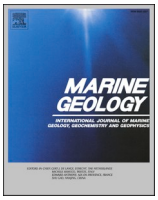

Research Article

Factors controlling rare earth element plus yttrium enrichment in Fe—Mn crusts from Canary Islands Seamounts (NE Central Atlantic)

E. Marino [a,*], F.J. González [a], T. Kuhn [b], P. Madureira [c,d], L. Somoza [a], T. Medialdea [a], A. Lobato [a], C. Miguel [e], J. Reyes [a], M. Oeser [f]

[a] Marine Geology Division, Geological Survey of Spain (CSIC-IGME), Ríos Rosas, 23, 28003 Madrid, Spain
[b] Federal Institute for Geosciences and Natural Resources (BGR), Stilleweg 2, D-30655 Hannover, Germany
[c] Dep. Geosciences and Institute of Earth Sciences of Évora University, 7000-671 Évora, Portugal
[d] Portuguese Task Group for the Extension of the Continental Shelf (EMEPC), 2770-047 Paço de Arcos, Portugal
[e] HERCULES Laboratory, IN2PAST Associate Laboratory and City University of Macau Chair in Sustainable Heritage, University of Évora, Palácio do Vimioso, Largo Marquês de Marialva 8, 7000-809 Évora, Portugal
[f] Leibniz Universität Hannover Institut für Mineralogie, Callinstraße, 3, 30167 Hannover, Germany

ARTICLE INFO

Editor: Shu Gao

Keywords:
Fe—Mn Crusts
High resolution analyses
Rare earth elements plus yttrium enrichment
Water masses influence

ABSTRACT

Marine minerals are important because concentrate in their structure high contents of strategic and critical elements as rare earth elements. Forty-two samples from eight seamounts of Canary Islands Seamount Province (CISP) have been analyzed in order to evaluate their rare earth elements plus yttrium contents (REY). Highest contents of REY are related to hydrogenetic minerals and essentially Fe-vernadite (on average 3000 μg/g). Diagenetic minerals, on the other hand, show the lowest REY contents with an average content of 260 μg/g. These differences also depend on the growth rates, hydrogenetic minerals with growth rates between 0.5 and 5 mm/Ma allow the incorporation of more REY in their structure. REY contents in studied samples varies depending several factors associated with depth and location, shallowest samples presumably growth near or within the oxygen minimum zone are the most enriched with up to 3800 μg/g due to local enrichment of these elements and the slowest growth rate promoted by the reduced ambient conditions while deeper samples around 3000 m water depth show 2800 μg/g. Location also has a role in REY contents essentially due to the presence of different currents. Samples faced to north are exposed to the more oxygenated waters of the North Atlantic Deep Water and are depleted in REY if compared with deeper samples facing to south to the more oxic Antarctic Bottom Water. Finally, the case of study made on three different seamounts of the CISP show that Fe—Mn crusts from this area could provide on average 130 tons of hydrometallurgical recovered REY (based on 1 km^2 areal crust coverage) together with interesting quantity of several other strategic and base elements as Mn, Co, Ni, Cu, V, Mo between others.

1. Introduction

Rare Earth Elements plus Yttrium (hereafter REY) are a group of chemical elements composed by the lanthanides and yttrium that usually can be found associated in the same ore (Haxel et al., 2002; Long et al., 2010). Scandium, present in most deposits of rare-earth compounds, is also included by the International Union of Pure and Applied Chemistry as a rare-earth element. REY have gained importance in the last 20 years due to their use in the development of new technologies, such as laptops, smartphones and tablets. Probably more important is their use in the development of more efficient electric turbines, e.g. Nd magnets used in windmills or hydro-electric power dams, but also as alloy metals in the development of superconductors, or in the production of better ceramics or glasses. Anyway, more than a half of REY are used as catalysts in the petroleum refinery that comprehend >20% of their consumption (The White House, 2021).

REY are not so rare in the continental crust as their name may suggest, but they are considered rare because they are hardly found in exploitable deposits (Haxel et al., 2002). Currently, the global production is led by China, with >80%, followed by Australia with almost 15%, while the remaining 5% is divided by the rest of producers. Land-based REY deposits are represented by different types like carbonatites,

* Corresponding author.
E-mail address: e.marino@igme.es (E. Marino).

https://doi.org/10.1016/j.margeo.2023.107144
Received 10 April 2023; Received in revised form 27 June 2023; Accepted 6 September 2023
Available online 17 September 2023

alkaline igneous rocks, skarns or enriched in sedimentary rock by the weathering of these deposits forming placers, bauxites and laterites (Lottermoser, 1990; Hedrick et al., 1997; Berger et al., 2014; Holtstam et al., 2014; Deady et al., 2016; Dostal, 2016; Verplanck et al., 2016; Santofimia et al., 2022; Gonzalez et al., 2023). The principal metal association of carbonatite is represented by Fe-Nb-REY minerals deposit and hydrothermal iron-oxides (Cu-Au-REE) (Mountain Pass, Bayan Obo, Olympic Dam mines), in which the main ores are represented by REY-rich phosphates, as monazite, bastnaesite, huanghoite (Drew et al., 1990; Chao et al., 1997; Fan et al., 2016). Placer deposits have been a source of REY in fluvial, beaches and shallow-water areas as monazite and xenotime bearing deposits formed by erosion and weathering of primary rocks (Chakhmouradian and Wall, 2012; Wall, 2013; Sakellariadou et al., 2022). Enrichment of these elements also occurs by ion-adsorption ores in lateritic weathering crusts developed on granitic and syenitic rocks in tropical environment and in secondary clay minerals (Haxel et al., 2002; Zhou et al., 2017).

Fe—Mn crusts on the deep-seafloor concentrate contents of REY with economic potential in their structure due to the slow absorption of mono- and di- carbonate complexes from seawater (Bau, 1996; Bau et al., 2014). Fe—Mn crusts can be found in all ocean basins covering different hard substrates on seamounts and plateaus, forming quite continuous pavements of up to 25 cm of thickness (Glasby, 1972; Halbach et al., 1981; Koschinsky and Halbach, 1995; Koschinsky et al., 1996; Hein et al., 1997, 2000; Rona, 2003; González et al., 2016; Marino et al., 2017, 2018, 2019). Fe—Mn crusts form essentially under the influence of hydrogenetic process, involving slow precipitation of colloidal Fe and Mn oxy-hydroxides during millions of years and concentrating high contents of LREE, especially Ce (Hein et al., 1988; Bau and Koschinsky, 2009; Bau et al., 2014; González et al., 2016; 2023; Sakellariadou et al., 2022; Benites et al., 2023). Sometimes, Fe—Mn crusts could show the influence of diagenetic processes when they are submitted to particular redox conditions or when the water-crust interface is blocked by sediments promoting a pore water precipitation that endorse a higher growth and a lower enrichment in REE. Ancient Fe—Mn crusts affected by phosphatization processes, especially extended during the Eocene-Miocene, can accumulate high contents of Y (Glasby et al., 1997; Hein et al., 1997, 2000; Usui et al., 2017; Kuhn et al., 2017; Marino et al., 2017, 2018). Hydrothermal formation of Fe—Mn crusts and stratabounds due to direct precipitation of oxy-hydroxides from hydrothermal fluids are usually very poor in REYs (Hein et al., 2005; González et al., 2016, 2020; Marino et al., 2019). Diagenetic and hydrothermal Fe—Mn minerals usually concentrate low contents of REY essentially due to their high growth rate (10–100 and 100–1000 and more mm/My respectively) that did not allow the absorption of these elements from the surrounding waters (Hein et al., 1997; González et al., 2009, 2010, 2012; Zawadzki et al., 2021).

This work is focused on evaluating of the REY contents in forty-two different studied samples of Fe—Mn crusts from the CISP area. We present a regional study on the distribution of REY proposing their mechanisms of enrichment in eight representative seamounts of the Canary Islands Seamounts Province (CISP). The main topic of the paper

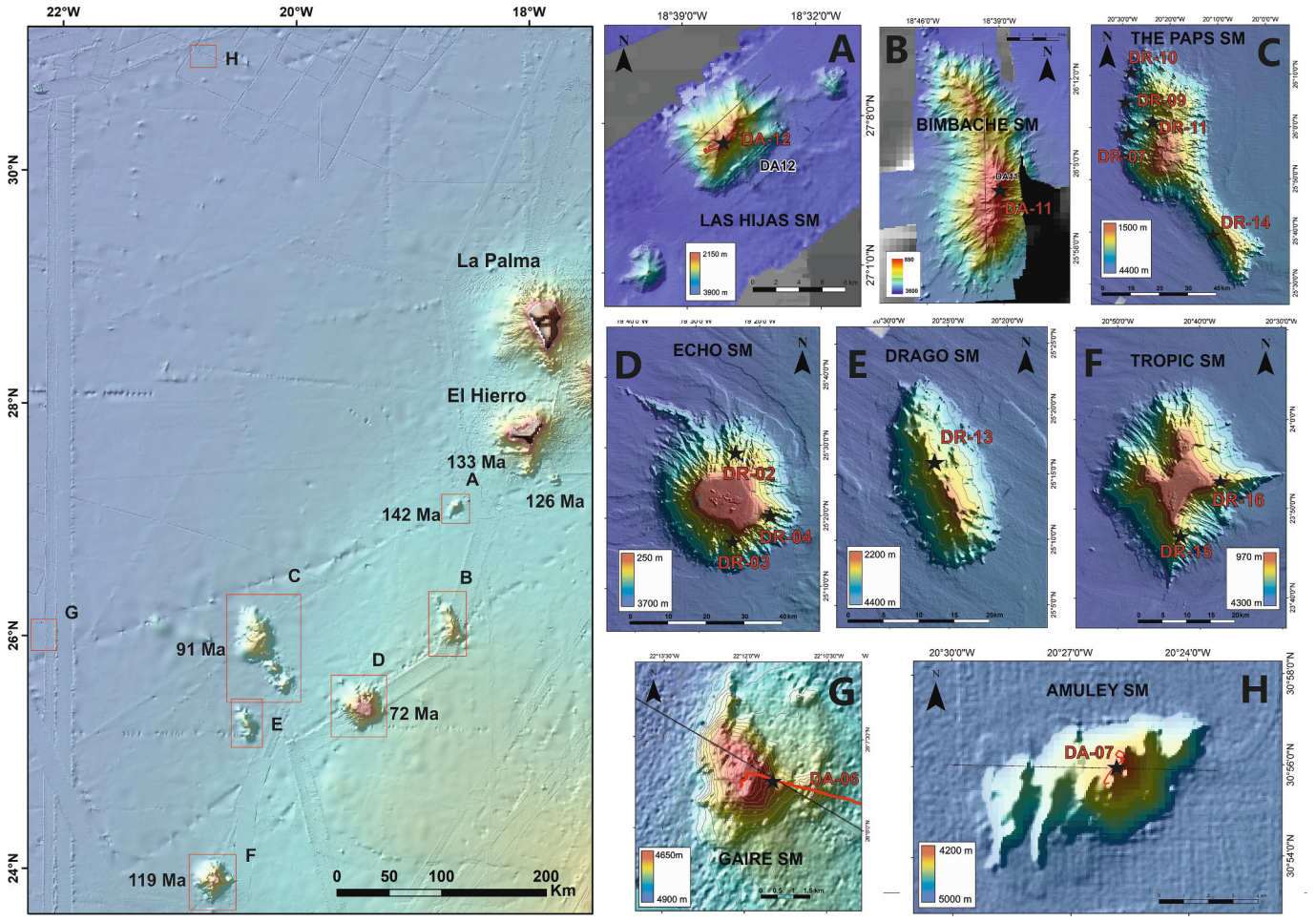

Fig. 1. Regional setting of the Canary Islands Seamounts Province (CISP). General bathymetric view of the study area on the left and zoom of the individual studied seamounts and their sampling sites on the right. The ages of principal seamounts are showed in the bathymetric mosaic: Henry Seamount (126 Ma), El Hierro South Ridge (133 Ma), Las Hijas Seamount (142 Ma), The Paps Seamount (91 Ma), Echo Seamount (72 Ma), Tropic Seamount (142 Ma), ages from van den Bogaard, 2013 and Somoza et al., 2015 (Echo age).

is to get better knowledge on how REY are concentrated in Fe—Mn crusts. To address the variation in REY contents we used high-resolution mineralogical and geochemical analyses and the application of statistical methods in order to highlight in which mineral phases REY are concentrated and what is their variability in accordance with water depth and different location on samples.

2. Geological and oceanographic setting

The study area is located west and southwest of the Canary Islands Archipelago, and comprises several seamounts at different depths ranging from 5000 to 3500 m at their base (Fig. 1)). These seamounts have a volcanic intraplate origin due to the presence of a mantle area anomalously hot (van den Bogaard, 2013). This mantle plume promoted a higher proportion of melting in the mantle and the rise of the magma leading to the formation of the Canary archipelago and of hundreds of seamounts. Geochemical dating methods based on $^{40}Ar/^{39}Ar$ age performed on different minerals show that their formation is placed in the Early Cretaceous period, after the opening of the Atlantic Ocean (van den Bogaard, 2013). The oldest age calculated in the area belongs to Las Hijas seamount (142 Ma) and similar ages have been also calculated in El Hierro Ridge and in the Henry seamount (respectively 133 and 126 Ma). Southern seamounts as The Paps and Tropic (respectively 91 and 119 Ma) show younger age of Late Cretaceous period. These data made CISP seamounts to be considered the oldest volcanic seamount track in the Atlantic Ocean (van den Bogaard, 2013). Seamounts of the CISP show variable morphology represented essentially by i) guyot type (Echo, Tropic), ii) ridge type (Bimbache, The Paps and Drago), iii) cone type (Las Hijas, Amuley and Gaire) (Fig. 2). Biggest seamounts also show the presence of secondary volcanic cones on the top (Echo) and the signs of old landslides in their flanks (Tropic, Echo, The Paps) (Fig. 2C, D, F) (Palomino et al., 2016). Seamount investigation is not only important for their formation and as source of minerals deposits but also due to their singular ecosystems in the oceans for the benthic fauna (Somoza et al., 2021).

REY elements can be concentrated in seawater from different sources such as continental shelf weathering, dust input, volcanic-hydrothermal sources or diagenetic alteration of the substrate rocks (Juteau et al., 1978; Hein et al., 2000; Maslennikov et al., 2003; Dubinin, 2004; Dubinin and Rozanov, 2001; Zhong et al., 2018). The presence of volcanic activity in the CISP since the Early Cretaceous is evident from the occurrence of the great amount of seamounts, the active volcanoes and submarine magmatic-hydrothermal systems development in the Canary Islands (van den Bogaard, 2013; Medialdea et al., 2017; Somoza et al., 2017; González et al., 2020; Klügel et al., 2020). Another source of REY in the study area came from the Saharan dust that moves each year tons of materials from the continent to the Atlantic Ocean. This dust can be transported for hundreds of kilometers to the west, reaching Canary

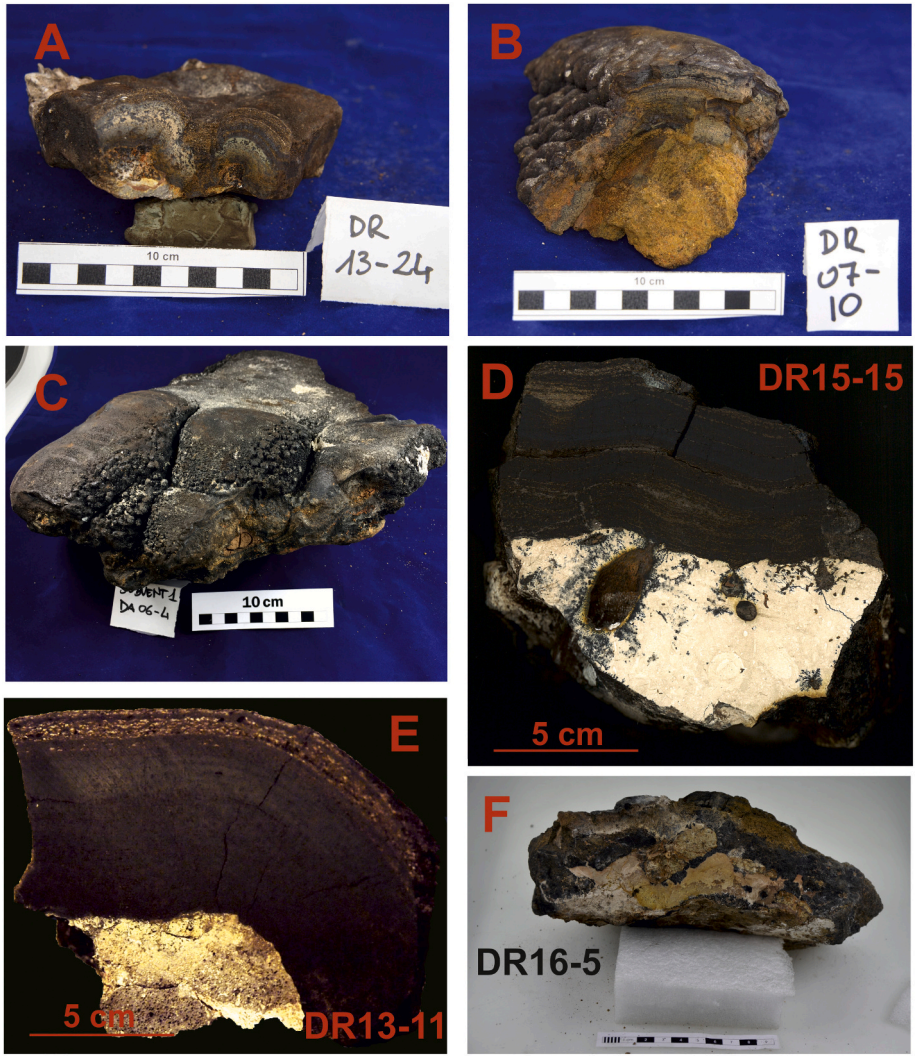

Fig. 2. Images of some of the selected Fe—Mn crust samples for this study. (A-D). Samples show different surface structure and lamination. Different substrates can be recognized: D) calcareous semiconsolidated rocks, E) altered volcanic breccia, F) phosphates.

Islands and the study area, as can be interpreted by the presence of Saharan sands, which are recognized from mineralogical and geochemical studies (Grousset et al., 1998; Grousset and Biscaye, 2005; Kandler et al., 2011; Lázaro et al., 2008; Muhs et al., 2010; Mendez et al., 2010). Moreover, the high contents of REY in Saharan sands can be linked to the presence of vast phosphate deposits located in the Western Sahara (Abed et al., 2009; Newman, 2011).

Within the study area it has been recognized the important role of several shallow and deep currents that mobilize water masses from north to south and also conversely from south to north (Sarnthein et al., 1982; Machín et al., 2006; Pastor et al., 2015; Marino et al., 2017). The most important currents at intermediate depths (between around 700 and 1000 m depths) are represented by the North Atlantic Central Water (NACW) and the South Atlantic Central Water (SACW) and Antarctic Intermediate Water (AAIW). The deepest currents are represented by the North Atlantic Deep Water (NADW) below water depths of 1500 m and the AABW below ~4000 m. Moreover, the study area shows the presence of a thick Oxygen Minimum Zone (OMZ) located between water depths of 100 and 700 m in the equatorial and tropical Atlantic Ocean. The lowest contents of oxygen (<50 μmol/kg) occur in the core of the OMZ and at 400–500 m deep (Brandt et al., 2010, 2012). The formation of this thick OMZ is due both to the dissolved oxygen (DO) of the currents that are ventilating the area, and also to the high biological activity resulting from upwelling currents (Brandt et al., 2010; Bashmachnikov et al., 2015). The OMZ concentrate several elements (Fe, Mn, Co, etc.) as reduced dissolved metals that can precipitate forming thick Fe—Mn crusts pavements due to oxidation promoted by the mixing of waters due to currents, which are potential sources for REY (Johnson et al., 1996; Hein et al., 2000, 2013; Marino et al., 2017; Zhong et al., 2018).

3. Sampling sites and methodology

In this work, 42 samples recovered by dredging from eight seamounts in the CISP have been studied. These samples were collected both at different depths and geographical location (Table 1 and Fig. 1). Extensive pavements of Fe—Mn crusts covering volcanic and sedimentary substrates have been discovered in the CISP (Vázquez et al., 2011; González et al., 2014; Marino et al., 2017). Hundreds of seamounts and submarine hills formed from extinct volcanoes rise abruptly from the seafloor at 4000–5000 m water depth. Amongst them we sample eight seamounts (Las Hijas, Bimbache, Echo, The Paps, Drago, Tropic, Gaire and Amuley) and recovered Fe—Mn crusts from them were studied using bulk and high-resolution mineralogical and chemical methods.

Laboratory mineralogical and geochemical analyses were performed at the General Laboratories of the Geological and Mining Institute of Spain (IGME-CSIC) and the National Centre of Electronic Microscopy (CNME-UCM), the HERCULES laboratory of Évora University (HERCULES-UÉ, Portugal) while some EPMA and the LA-ICP-MS were performed in collaboration with the Institute for Mineralogy of the Leibniz University Hannover (LUH, Germany) and the Federal Institute for Geosciences and Natural Resources of Hannover (BGR, Germany).

General mineralogical and petrographic analyses were conducted at

Table 1
Resume table of Fe—Mn crusts from CISP including location, dredge depth, average depth of the samples and thickness.

Sample	Cruise	Seamount	Latitude	Longitude	Water depth (m)	Avrg. Depth	Thickness (mm)
DR02–9	DRAGO0511	Echo	25° 29,62′N	19° 23,47′W	1890–1875	1880	50
DR02–10	DRAGO0511		25° 29,62′N	19° 23,47′W	1890–1875	1880	27
DR03–1	DRAGO0511		25° 15,10′N	19° 23,55′W	1949–1757	1800	30
DR04–14	DRAGO0511		25° 19,51′N	19° 18,92′W	1832–1593	1600	35
DR04–15 A	DRAGO0511		25° 19,51′N	19° 18,92′W	1832–1593	1600	25
DR07–8	DRAGO0511	The Paps	25° 57,18′N	20° 21,73′W	1860	1860	80
DR07–9	DRAGO0511		25° 57,18′N	20° 21,73′W	1860	1860	58
DR07–10	DRAGO0511		25° 57,18′N	20° 21,73′W	1860	1860	85
DR07–11	DRAGO0511		25° 57,18′N	20° 21,73′W	1860	1860	50
DR07–12	DRAGO0511		25° 57,18′N	20° 21,73′W	1860	1860	110
DR09–10	DRAGO0511		26° 00,80′N	20° 21,57′W	2340–2198	2300	20
DR09–11	DRAGO0511		26° 00,80′N	20° 21,57′W	2340–2198	2300	60
DR09–20	DRAGO0511		26° 00,80′N	20° 21,57′W	2340–2198	2300	45
DR09–21	DRAGO0511		26° 00,80′N	20° 21,57′W	2340–2198	2300	35
DR09–22	DRAGO0511		26° 00,80′N	20° 21,57′W	2340–2198	2300	48
DR10–7	DRAGO0511		26° 07,09′N	20° 19,75′W	3010–2839	2900	60
DR10-10A	DRAGO0511		26° 07,09′N	20° 19,75′W	3010–2839	2900	34
DR10-10B	DRAGO0511		26° 07,09′N	20° 19,75′W	3010–2839	2900	18
DR11–1	DRAGO0511		25° 57,68′N	20° 19,18′W	1957–1952	1950	15
DR11–2	DRAGO0511		25° 57,68′N	20° 19,18′W	1957–1952	1950	30
DR14–1	DRAGO0511		25° 39,25′N	20° 07,45′W	2221–2157	2180	30
DR14–3	DRAGO0511		25° 39,25′N	20° 07,45′W	2221–2157	2180	15
DR13–11	DRAGO0511	Drago	25° 13,60′N	20° 24,90′W	2426–2290	2300	35
DR13–12	DRAGO0511		25° 13,60′N	20° 24,90′W	2426–2290	2300	110
DR13–13	DRAGO0511		25° 13,60′N	20° 24,90′W	2426–2290	2300	85
DR13–21	DRAGO0511		25° 13,60′N	20° 24,90′W	2426–2290	2300	94
DR13–22	DRAGO0511		25° 13,60′N	20° 24,90′W	2426–2290	2300	47
DR13–23	DRAGO0511		25° 13,60′N	20° 24,90′W	2426–2290	2300	43
DR13–24	DRAGO0511		25° 13,60′N	20° 24,90′W	2426–2290	2300	35
DR13–25	DRAGO0511		25° 13,60′N	20° 24,90′W	2426–2290	2300	38
DR15-14 A	DRAGO0511	Tropic	23° 46,18′N	20° 43,17′W	2287–2263	2270	70
DR15–15	DRAGO0511		23° 46,18′N	20° 43,17′W	2287–2263	2270	70
DR16–13	DRAGO0511		23° 52,91′N	20° 37,07′W	1719	1719	90
DR16–14	DRAGO0511		23° 52,91′N	20° 37,07′W	1719	1719	100
DR19–1	DRAGO0511		23° 51,81′N	20° 46,26′W	2311–1272	1800	29
DA06–1	SUBVENT1	Gaire	26°06.20′ N	22°09.00′W	4823	4823	120
DA06–2	SUBVENT1		26°06.20′ N	22°09.00′W	4823	4823	78
DA06–4	SUBVENT1		26°06.20′ N	22°09.00′W	4823	4823	64
DA06–7	SUBVENT1		26°06.20′ N	22°09.00′W	4823	4823	45
DA07–1	SUBVENT1	Amuley	30°56.12′ N	20°25.66′W	4200	4200	68
DA11–8	SUBVENT1	Bimbache	26°03.11′N	18°39.47′W	1840–1165	1450	30
DA12–11	SUBVENT1	Las Hijas	27°07.37′N	18°36.37′W	3720–2200	3100	28

IGME-CSIC on polished thin sections (ca. 30–120 μm thick) using a DM2700P Leica Microscope (Leica, Wetzlar, Germany) coupled to a DFC550 digital camera. X-ray powder diffraction (XRD) method was performed using a PANalytical X'Pert PRO diffractometer (Philips Analytical, Almelo, The Netherlands), with CuKα radiation, carbon monochromator and automatic slit. The analytical conditions were: CuKα radiation at 40 kV and 30 mA, a curved graphite secondary monochromator, scans from 2 to 70° (2θ), step size of 0.0170° (2θ) and step time 0.5°/min.

Raman analyses were performed at HERCULES-UÉ with a Raman spectrometer HORIBA XPlora (Horiba, Ltd., Kyoto, Japan) equipped with a diode laser of 28 mW operating at 785 nm, coupled to an Olympus microscope (Tokyo, Japan). Raman spectra were acquired at room temperature in extended mode in the 100–1000 cm^{-1} region, where most of Fe—Mn oxyhydroxides peaks are identifiable. The laser was focused with an Olympus 50× lens, with 1.1–2.8 mW laser power on the sample surface. Several exposure times and number of accumulation cycles have been tested. The best results were reached using 10 s of exposure time, 50 to 100 cycles of accumulation and a 600 g/mm diffraction grating that provides high signal intensity and the best Raman bands resolution, using the LabSPEC5 software designed for HORIBA.

Electron probe micro-analyser (EPMA) analyses were performed at CNME-UCM on polished thin sections using a Jeol JXA-8900 M Electron Probe WDS/EDS Micro Analyser (JEOL, Tokyo, Japan), operating at 15–20 kV and 50 mA, operating at 15 kV, equipped with four wavelength dispersion spectrometers in which these crystals were placed, as follows: channel 1: TAP; channel 2: LIF; channel 3: PETJ; channel 4: PETH. Several standards were used to calibrate the analyses: pure metals, synthetic and natural minerals, all from international suppliers. The EPMA also allow to collect Back-scattered electron images of the different spot analyses. Electron probe micro-analyser (CAMECA SX 100 and JEOLJXA-8530F, CAMECA, Paris, France, JEOL, Tokyo, Japan) was used in the BGR laboratory. Analyses were made on polished thin sections at 15/20 kV accelerating voltage and 40 nA beam current. The single layers were analyzed with a focused (1–5 μm) and a defocused (5–20 μm) beam. Counting times for the analyzed elements were 10s for Mn, Fe, Ni, Cu, Na, Mg, Al, Si, K, Ca, Ti, P, S, Cl, 40s for V, 45 s for Pb, 50s forCo, 90s for Zn, 100 s for Ba, Mo and Sr and 110 s for Ce.

Bulk geochemistry of major elements was determined at IGME-CSIC using X-Ray Fluorescence (XRF), PANalytical's ZETIUM (Malvern Panalytical, Almelo, The Netherlands) equipment with a rhodium tube and fused pearl preparation (SuperQ, Malvern Panalytical, Almelo, The Netherlands). The accuracy of the data was verified using international standard NOD-A-1 (USGS), and precision was found to be better than ±5%. Analytical conditions were 50 kV voltage and 50 mA. The obtained contents were compared with certified international standards. Na was measured using a Varian FS-220 atomic absorption spectrometer (Varian Inc., Palo Alto, CA, USA) and loss on ignition (LOI) was determined by calcination at 950 °C. Trace (Be, V, Cr, Ni, Cu Zn, As, Se, Mo, Cd, Sb, Te, Ba, Tl, Pb, Th, U) and REY elements were performed using coupled plasma mass spectrometry (ICP-MS) (AGILENT 7500 ce, Agilent Technologies, Santa Clara, CA, USA) and Inductively Coupled Plasma Atomic Emission Spectroscopy (ICP-AES) (Varian Vista-MPX, Varian Inc., Palo Alto, CA, USA) measurements for Co and Ni. For these techniques, samples were prepared with an ultrapure 3-acid digestion (HF, HNO_3, and HCl), dried afterwards until almost complete dryness and the residuals were diluted with HCl 10%.

Trace element concentrations of spot analyses on Fe—Mn crusts were acquired at LUH by femtosecond-Laser Ablation-ICP-MS employing a fast scanning sector field ICP-MS (Thermo Scientific Element XR, Thermo Fisher Scientific, Waltham, MA, USA) coupled to a Spectra Physics (Santa Clara, CA, USA) Solstice 194 nm femtosecond laser ablation system at the Institute of Mineralogy at the Leibniz University of Hannover (Hannover, Germany). Details of the fs-LA system are described in (Oeser et al., 2014; Lazarov and Horn, 2015; Collinet et al., 2017; Neave et al., 2018). In the present study, sample material was ablated along lines with a laser spot size of 40 μm in diameter and a scanning speed of 20 μm/s. Laser repetition rate was 20 Hz. Each analysis consisted of 30 s background acquisition and 60–80 s ablation interval. Ablated material was transported with a He gas stream towards the ICP-MS and mixed with Ar before entering the torch. The ICP-MS was operated in low mass resolution mode and the following isotopes were analyzed: 7Li, 27Al, 43Ca, 55Mn, 57Fe, 59Co, 60Ni, 63Cu, 66Zn, 69Ga, 75As, 77Se, 89Y, 90Zr, 93Nb, 95Mo, 121Sb, 125Te, 139La, 140Ce, 141Pr, 143Nd, 147Sm, 153Eu, 157Gd, 159 Tb, 163Dy, 165Ho, 167Er, 169Tm, 172Yb, 175Lu, 177Hf, 181Ta, 208Pb, 232Th, 238 U. ThO-Th ratios were monitored and found to be always <0.4%, indicating that oxide formation rates were negligible. The precision of the technique is better than 1.5% and the accuracy is better than 1.6%. External calibration of the acquired data was performed using the USGS reference glasses BCR-2G with the preferred values reported in the GeoReM database (Jochum et al., 2007), or using NIST SRM 610 (Jochum et al., 2011). Data reduction was performed with the Lotus-based spreadsheet program LAMTRACE (Jackson, 2008), where 27Al was used for internal standardization.

The age of the Fe—Mn crust samples was calculated using the empirical Co-chronometer method established by Manheim and Lane-Bostwick (1988) with bulk chemical compositions.

$$GR\ (mm/Ma) = 0.68/Co_n^{1.67} \rightarrow Co_n = Co\%\text{x}\ 50/(Fe\% + Mn\%)$$

This method has the limitation that does not consider the presence of possible hiatuses or erosion during the growth of the Fe—Mn crusts. Therefore, calculated ages have to be considered as minimum values while the growth rates represent the maximum values (Ingram et al., 1990).

4. Results

4.1. Physical properties and textural features

Studied samples (Table 1) represent fragments of Fe—Mn crusts pavements recovered from the studied seamounts (Las Hijas, Bimbache, The Paps, Echo, Drago, Tropic, Gaire and Amuley). These fragments show variable size from 3 cm up to 30 cm and thickness variable from few mm up to 20 cm. Surface morphology ranges from microbotryoidal-smooth flat to botryoidal, the latter presenting botryoids size ranging from 1 to 2 mm up to 5 cm, and a great variety of mixed types (Fig. 2). Fe—Mn crusts are fragile and porous, usually dark colored (from dark brown to black), with a general matte luster, although in some samples is possible to identify a metallic luster in naturally polished surfaces. In cross sections, crusts are formed by the accretion of very thin parallel to sub-parallel laminae (< 1 mm), packed in layers that enclose laminae with similar colour and texture with variable thickness (0,5–2 cm) (Fig. 2A, B, D, E). Within the lamination it is possible to identify light colored laminae (white to beige) formed by silicate-carbonate sediments and bioclasts or authigenic phosphates (Fig. 2E). Substrates on which Fe—Mn crusts growth are variable from altered basalts, calcareous semiconsolidated sediments, altered volcanic breccia and phosphates (Fig. 2D-F).

Samples show different morphological features and thickness depending on their depth and location on the seamount. Shallowest samples (< 2000 m) formed near the top of the seamount are usually thinner with an average thickness of 27 mm with poor presence of elongated botryoids, belonging essentially to Echo and The Paps seamounts. (Fig. 2A). The second range of average depths is located between 2000 and 2500 m that correspond to most samples of this work. The average thickness is 61 mm with three samples reaching 100 mm or more (DR07–12, DR13–12 and DR16–14) from The Paps, Drago and Tropic seamounts. Samples from this range are usually botryoidal (essentially from The Paps Seamount) even if some can also show

smooth surfaces (Table 1, Fig. 2B, E). Finally, the last thickness range comprises all those samples with an average depth of over 2500 m. At these depths were collected samples from one of the dredges obtained in The Paps, from Gaire, Amuley and Las Hijas, with an average thickness of 65 mm and essentially smooth surface or with the presence of small botryoids on the sides protected from the influence of ocean currents (Fig. 2C).

Under the petrographic microscope (reflected light) Fe—Mn crusts appear grey colored with low or no pleochroism and high porosity (up to 60%). Microscopic studies allow to differentiate two main texture in CISP Fe—Mn crusts: i) columnar to dense parallel and ii) dendritic to mottled. Both structures can be found in all the studied samples in different proportions (Fig. 3). The transition between these two main structures shows different features and could be found as an abrupt change after a discontinuity (Fig. 3C) or with a gradual change (Fig. 3D). In studied samples there is no clear relationship between depth and main structure even if it is possible to highlight that deepest samples show a massive lamination if compared with shallower samples (Fig. 3B, C). Internal structures are mostly related to the position of the crust pavement on the seamount. In this way, samples collected in the south flank of the seamounts (e.g. DR04–14 and DR16–14) show a prevalence of dense/columnar structure, while samples collected on the north flank of the seamount (e.g. DR07–9 and DR10–7) show a prevalence of dendritic/mottled structure (Fig. 3).

Within the lamination it was also possible to identify several detrital grains (essentially quartz with less feldspars and calcite or magnetite/ilmenite), usually accumulated in the inter-columnar space or in the mottled-dendritic layers, and also the presence of different foraminifera and coccoliths (Fig. 3E, F).

4.2. Bulk mineralogy

All samples were studied with powder X-Ray diffraction method showing that main Fe and Mn minerals have a low crystallinity and broad reflections that sometimes are masked by the presence of well-crystallized detrital minerals such as quartz, feldspar, calcite or authigenic carbonate fluorapatite (CFA). Predominant Mn minerals are vernadite, which reflections at 2.45 and 1.42 Å, and birnessite that usually overlap vernadite reflections while its main reflection at 7 Å is not present or is masked in the basal noise (Fig. 4).

In some samples (e.g. DR02–10, DR07–8, DR09–10) it is possible to identify small and broad 9–10 Å and 4.8–4.5 Å peaks that belong to the

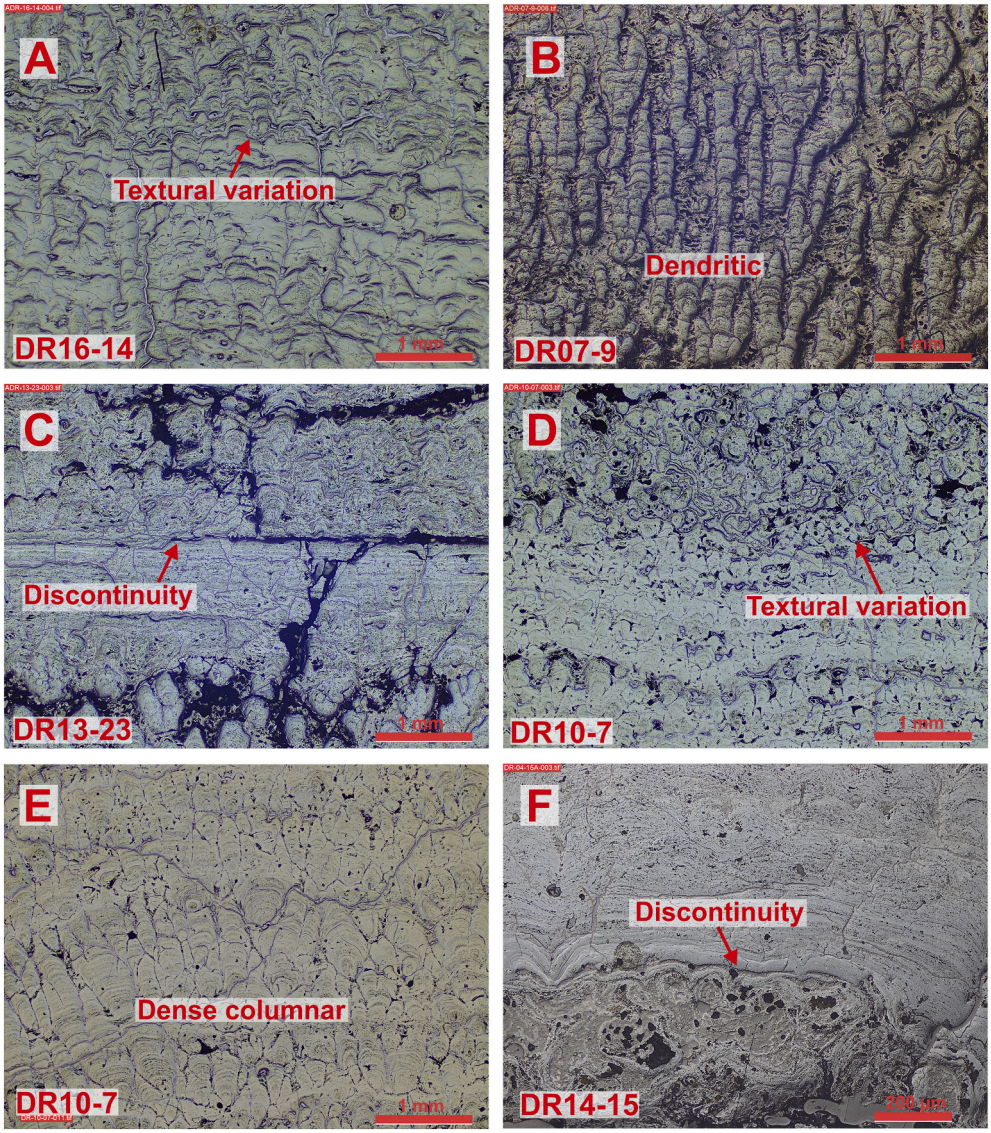

Fig. 3. Petrographic microscope image of thin polished samples (*E*-H) in which it is possible to differentiate: A, E) columnar/dense, B, C, D) dendritic and mottled structures and discontinuity within the lamination.

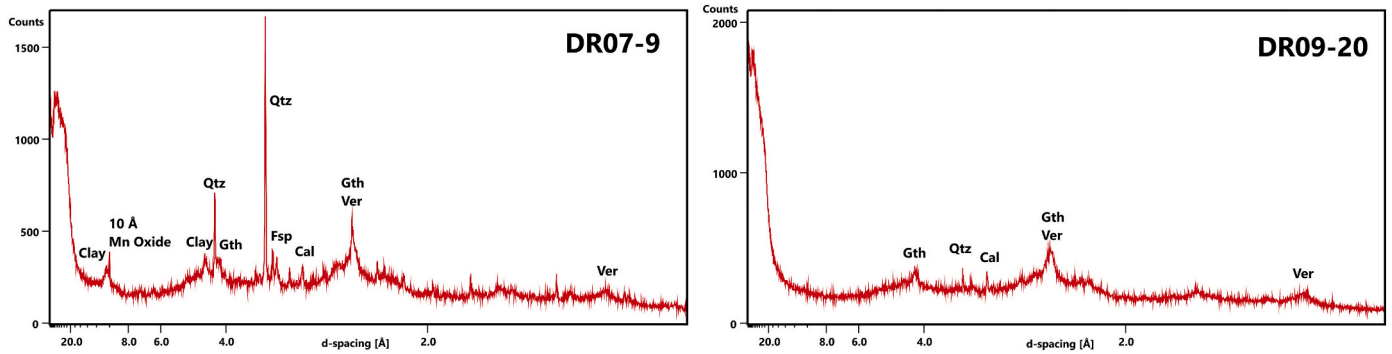

Fig. 4. X-Ray Diffraction (XRD) analysis of bulk selected samples. In both samples it is possible to recognize Fe-oxyhydroxides represented by goethite group (Gth) minerals and Mn-oxides essentially Fe-vernadite (Ver) and birnessite (Bir). In sample DR07–9, it is also possible to recognize ~10 Å reflection due to the presence of todorokite (Tod), asbolane (Asb) or buserite (Bus).

001 and 002 reflections of diagenetic Mn minerals such as todorokite, asbolane or buserite. Fe oxyhydroxides are represented by goethite group minerals, whose reflections are at 4.2 and 1.4 Å and metastable phases as feroxyhyte and ferrihydrite that are masked in the broad goethite peaks (Fig. 4). Minor minerals are represented by quartz, feldspars, calcite, CFA, clays and sometimes magnetite/ilmenite.

4.3. Bulk geochemistry

4.3.1. Major and trace elements

The geochemistry of the studied Fe—Mn crusts is in accordance with mineralogical data, with the highest contents represented by Fe and Mn (in average 25 and 17 wt% respectively) and an average Mn/Fe ratio of 0.8 (varying from 0.5 and 1) (Table 2). Silica related elements (Si, Al, Mg, K, Ca and Na) sum in average around 10 wt% with the highest contents represented by Si and Al (maximum of 9.1 and 3.4 wt% respectively). Ca show an average content of 3 wt% but in sample DR11–2 reach the maximum of 18 wt% due to the presence of detrital carbonates observed within the lamination. In other samples (e.g. DR04–15 or DR13–11) the high contents of Ca (up to 8,7 wt%). This element is also coupled with high P that in these samples reach 3.9 wt% due to the presence of CFA and the average values of all the samples reach 0.7 wt% (Table 2, Supp. Table 1).

CISP Fe—Mn crusts also show high contents of several strategic and critical elements. The highest values are represented by Co with an average content of 5000 μg/g and a maximum of 8400 μg/g, followed by Ni, Pb, Ba, V, Cu, Zn and Mo (in average 2400, 1500, 1460, 990, 620, 520 and 450 μg/g respectively. The total content of all potential ore metals (Cu, Co, Ni, V, Zn and Mo) sum in average 1 wt% with maximum contents of 1.4 wt% in the richest samples. The contents of other elements like Sb (56 μg/g), Tl (98 μg/g) and especially Te (in average 41 μg/g with a maximum of 65 μg/g), are significant for their value as rare elements. The average sum of selected valuable elements (Co, Ni, Cu, V, Mo, Tl and Te) varies between 7200 μg/g in the Gaire Seamount samples and 10,200 μg/g in Tropic Seamount samples, with the minimum (4700 μg/g) reached in the only sample of the Amuley Seamount. CISP average geochemical data have been normalized to the values of the continental crust, the result showing that the Mn-related elements (e.g., Te, Co, Mo, Ni, Ce) have 1 to 3.5 magnitude order enrichment, while the Fe-related elements have 1 to 1.5 enrichment (Fig. 5). The most enriched element is Te with 4000 times more with respect the continental crust, followed by Co (500 times). On the other hand, Si related elements show no enrichment (Ca and Na) or a depletion reaching almost one magnitude order less (Si) (Fig. 5).

4.4. REY

REY bulk contents have been obtained from all studied samples using ICP-MS (Supp. Table 1). Their results have been summarized in Table 2. The average ΣREY is 3000 μg/g varying from 1500 to 3800 μg/g, and the highest contents are represented by the light rare earth elements (LREE) (La, Ce, Pr, Nd, Sm, Eu, and Gd) that in average reach a total of 2700 μg/g. Ce shows the highest concentration in CISP Fe—Mn crusts amongst all the LREE (up to 2300 μg/g), followed by La and Nd (respectively up to 490 and 430 μg/g). Heavy REY (HREY), on the other hand, show less contents with an average of 360 μg/g and reaching contents of 470 μg/g and a percentage with respect to the total REY varying from 7.4 to 22%.

The normalization of REY to the continental crust show a similar enrichment for all of them and about 10 to 20 times in CISP Fe—Mn crusts (Fig. 5). Furthermore, the normalization to the Post Archean Australian Shales (PAAS), typical standard for marine environments, show that all samples have a similar pattern, with a positive Ce anomaly and negative Y anomaly (Fig. 6). In this way we show the normalization of all the studied samples (Fig. 6A) and separately only samples with high contents of phosphates (Fig. 6B). In this figure is possible to see that some samples show less positive Ce anomaly or, in a particular case (DR07–8), a slightly positive Y anomaly.

4.5. High-resolution mineralogy and geochemistry

High-resolution mineralogy using micro-Raman analysis was performed in selected samples in order to identify the mineralogy of the single analyzed laminae (Fig. 7A-C). Results show the presence of the characteristic Raman bands of todorokite, asbolane/buserite and vernadite. The todorokite Raman spectrum shows a narrow peak around 650 cm^{-1} (643–647 cm^{-1}) and two other peaks at around 295 and 359 cm^{-1} (Fig. 7A). On the other hand, asbolane/buserite Raman spectrum shows several overlapped peaks especially at around 480, 500, 600 and 660 cm^{-1}, characteristic of this compound (Fig. 7B). Finally, vernadite was identified based on its characteristic Raman bands around 610 cm^{-1} and a shoulder around 560 cm^{-1}. This mineral is usually mixed with birnessite, of which characteristic Raman bands are present at 480, 550 and 670 cm^{-1} (Fig. 7C). Several layer-by-layer analyses made in-situ on polished thin sections have revealed that these CISP Fe—Mn crusts are formed essentially by low crystalline vernadite in up to 90% but it is also possible to individualize the presence of thin laminae, recognized with EPMA images (<100 μm) formed by asbolane/buserite and or todorokite (Fig. 7D, E). Spot analysis performed both with EPMA and with LA-ICP-MS confirmed the chemical differences between these minerals (Tables 2 and 3).

Microprobe geochemical analyses were performed on thin polished sections of 10 different samples from all the major seamounts of the CISP.

Table 2
Bulk chemical composition of the studied CISP Fe—Mn crusts from CISP normalized to 0% H2O. LOI = Loss on Ignition, Σ Val. Met. = Sum of other valuable metals (Cu, Co, Ni, V, Zn and Mo), N = number of samples.

	Echo				The Paps				Drago			
	N	Mean	Min	Max	N	Mean	Min	Max	N	Mean	Min	Max
Si (Wt%)	5	4.1	2.5	5.8	17	5.0	2.1	9.7	8	3.9	3.1	5.7
Al	5	1.9	1.4	2.7	17	2.1	1.1	3.5	8	1.9	1.6	2.4
Fe	5	25	23	26	17	24	14	28	8	25	19	29
Ca	5	3.1	2.2	5.5	17	3.7	1.9	18.0	8	4.2	2.1	8.7
Ti	5	1.0	0.8	1.5	17	1.0	0.6	1.3	8	1.0	0.9	1.2
Mn	5	17	14	18	17	17	8	21	8	17	12	19
K	5	0.5	0.4	0.7	17	0.5	0.2	0.8	8	0.5	0.4	0.8
Mg	5	1.6	1.3	1.8	17	1.6	1.1	2.7	8	1.4	1.2	1.7
P	5	0.8	0.5	1.4	17	0.6	0.4	1.6	8	0.9	0.4	2.8
Na	5	1.4	1.2	1.6	17	1.5	0.8	1.9	8	1.4	1.1	1.8
LOI	5	25	23	27	17	25	21	31	8	25	22	26
H_2O	5	14.8	10.7	21	17	14.2	6	23.4	8	14.2	7.1	22.4
Mn/Fe	5	0.79	0.70	0.92	17	0.82	0.53	1.04	8	0.79	0.70	0.88
ΣSi related el.	5	13	9	15	17	14	8	24	8	13	10	20
Be (μg/g)	5	11.55	9.31	13.63	17	10.20	3.33	13.43	8	10.80	9.40	13.56
V	5	1078	856	1195	17	936	404	1206	8	1052	899	1288
Cr	5	28.5	15.8	48.8	17	24.8	17.6	54.0	8	30.9	21.7	40.0
Co	5	4830	4077	5414	17	5202	3194	7700	8	5265	3659	6387
Ni	5	2345	1852	2996	17	2552	891	4430	8	2457	2086	3711
Cu	5	471	207	602	17	650	286	1016	8	667	511	794
Zn	5	545	468	613	17	521	200	683	8	538	469	640
As	5	413	364	439	17	373	194	459	8	389	331	482
Se	5	32.88	26.76	37.28	17	32.75	12.04	44.80	8	40.24	35.36	45.73
Mo	5	443	346	497	17	418	81	606	8	482	335	615
Cd	5	2.1	1.6	2.6	17	2.8	0.5	5.6	8	3.2	2.0	8.6
Sb	5	53.5	46.7	59.1	17	56.3	40.1	86.5	8	62.9	52.5	85.0
Te	5	42.9	33.1	47.3	17	42.8	25.5	60.3	8	48.9	41.2	56.8
Ba	5	1483	1115	1746	17	1329	429	2011	8	1549	1116	1995
Tl	5	85.23	68.44	101.51	17	104.59	41.18	140.74	8	98.81	77.79	113.38
Pb	5	1761	1422	1989	17	1537	564	2026	8	1480	1222	1932
Th	5	50.84	40.62	59.70	17	56.45	29.56	80.92	8	67.06	55.75	78.92
U	5	14.14	12.12	15.75	17	13.25	5.46	16.54	8	12.30	9.74	15.18
Y	5	218	199	239	17	210	120	264	8	234	175	285
La	5	353	305	397	17	345	172	485	8	393	324	456
Ce	5	1791	1663	1913	17	1665	692	2200	8	1839	1283	2155
Pr	5	76	63	88	17	74	34	105	8	87	69	101
Nd	5	312	260	360	17	304	143	432	8	356	285	417
Sm	5	63	53	73	17	62	29	87	8	73	57	85
Eu	5	15.3	13.0	17.7	17	15.0	6.9	21.2	8	17.5	14.0	20.6
Gd	5	73.3	62.9	82.1	17	71.2	35.8	98.2	8	80.9	65.5	93.9
Tb	5	10.3	8.9	11.6	17	10.1	5.0	14.0	8	11.5	9.1	13.4
Dy	5	60.4	54.2	66.3	17	59.0	29.3	81.4	8	65.9	51.9	76.4
Ho	5	11.9	11.1	12.8	17	11.5	5.8	15.6	8	12.6	10.0	14.7
Er	5	33.3	30.8	35.8	17	32.1	16.4	43.6	8	34.9	27.4	41.3
Tm	5	4.6	4.3	5.0	17	4.5	2.4	6.1	8	4.8	3.8	5.6
Yb	5	29.0	26.7	31.1	17	28.3	15.3	37.2	8	30.2	23.9	34.8
Lu	5	4.3	3.9	4.8	17	4.2	2.3	5.4	8	4.4	3.5	5.2
ΣREY	5	3056	2886	3283	17	2895	1447	3813	8	3245	2532	3675
GR(mm/Ma)	5	1.81	1.23	2.43	17	1.52	0.88	2.64	8	1.61	0.79	2.62
Age (Ma)	5	20	12	30	17	33	10	83	8	42	16	90
ΣVal. Met. (μg/g)	5	9295	7823	10,830	17	9906	5631	12,790	8	10,071	7933	12,083

	Tropic				Gaire				Amuley	Bimbache	Las Hijas
	N	Mean	Min	Max	N	Mean	Min	Max	DA07–1	DA11–8	DA12–11
Si (Wt%)	5	2.8	1.7	3.8	4	4.6	3.1	6.9	9.6	4.5	10.1
Al	5	1.3	0.7	1.6	4	2.3	1.8	3.0	2.7	2.6	4.3
Fe	5	27	27	28	4	24	21	26	20	26	23
Ca	5	3.3	2.5	4.4	4	1.6	1.4	1.8	1.5	4.9	4.6
Ti	5	0.9	0.7	1.2	4	0.7	0.6	0.7	0.7	1.0	1.6
Mn	5	19	17	22	4	17	16	17	14	18	13
K	5	0.3	0.3	0.4	4	0.5	0.4	0.7	0.8	0.5	1.0
Mg	5	1.3	1.1	1.5	4	1.3	1.2	1.6	1.1	1.9	1.5
P	5	0.7	0.5	1.2	4	0.4	0.4	0.4	0.3	0.7	0.9
Na	5	1.4	1.2	1.6	4	1.1	1.0	1.2	1.3	1.3	1.7
LOI	5	25	23	27	4	24	23	25	22	24	19
H_20	5	15	11.6	20	4	6.7	6.1	7	5.5	23.3	20.4
Mn/Fe	5	0.84	0.72	0.94	4	0.77	0.72	0.86	0.76	0.91	0.69
ΣSi related el.	5	10	8	12	4	12	9	15	17	16	23
Be (μg/g)	5	10.64	9.37	11.75	4	8.07	6.91	8.95	8.26	11.59	8.52

(*continued on next page*)

Table 2 (*continued*)

	Tropic				Gaire				Amuley	Bimbache	Las Hijas
	N	Mean	Min	Max	N	Mean	Min	Max	DA07–1	DA11–8	DA12–11
V	5	1109	923	1266	4	894	718	1044	666	1193	848
Cr	5	25.7	17.8	35.7	4	17.6	11.8	24.9	11.3	28.4	25.0
Co	5	5676	4054	8347	4	2965	2583	3194	1361	5904	3254
Ni	5	2293	1866	2919	4	1903	1399	3030	1343	2153	1611
Cu	5	452	258	647	4	818	441	1429	814	316	536
Zn	5	558	511	649	4	432	400	459	437	468	478
As	5	418	330	489	4	312	246	357	247	506	298
Se	5	35.20	26.97	41.95	4	37.15	31.49	43.37	24.92	34.63	31.57
Mo	5	535	440	648	4	492	401	570	462	488	286
Cd	5	2.2	1.5	2.9	4	3.2	2.2	4.3	2.3	3.4	2.6
Sb	5	67.5	55.2	88.7	4	41.7	33.8	47.2	39.0	62.6	40.6
Te	5	44.7	33.4	63.7	4	26.0	19.2	36.4	12.2	51.6	25.4
Ba	5	1658	1300	1998	4	1494	1265	1698	1741	1508	1362
Tl	5	101.71	65.70	130.37	4	97.11	76.50	121.86	45.68	142.72	59.22
Pb	5	1577	1258	1868	4	1124	915	1311	827	2366	1146
Th	5	58.44	48.13	80.86	4	155.93	115.12	188.51	119.93	53.46	48.53
U	5	12.06	9.13	14.54	4	10.31	9.07	11.55	7.73	16.46	12.69
Y	5	210	173	246	4	164	142	198	97	228	214
La	5	384	316	426	4	285	222	334	212	364	309
Ce	5	1954	1661	2230	4	2012	1572	2284	1789	1846	1494
Pr	5	86	67	97	4	77	61	93	56	79	69
Nd	5	349	277	392	4	304	239	366	221	326	284
Sm	5	72	58	79	4	68	54	83	51	67	58
Eu	5	17.1	14.0	18.8	4	15.9	13.0	19.5	11.6	16.0	14.6
Gd	5	78.9	68.1	84.8	4	70.0	57.1	84.7	50.1	74.9	67.5
Tb	5	11.2	9.9	12.1	4	10.1	8.2	12.3	7.2	10.7	9.7
Dy	5	64.1	59.7	68.9	4	55.6	46.1	67.7	38.2	64.6	57.3
Ho	5	12.1	11.1	12.9	4	10.0	8.4	12.2	6.9	12.9	11.0
Er	5	33.3	29.6	35.1	4	27.3	23.2	33.2	18.7	36.7	31.4
Tm	5	4.6	4.1	4.9	4	3.8	3.3	4.6	2.7	5.0	4.4
Yb	5	29.0	25.1	30.7	4	24.4	21.3	28.7	17.5	32.2	27.8
Lu	5	4.2	3.5	4.6	4	3.6	3.2	4.2	2.6	4.9	4.1
ΣREY	5	3308	2836	3666	4	3130	2475	3468	2581	3167	2655
GR(mm/Ma)	5	1.79	0.85	2.65	4	3.69	3.46	4.00	10.18	1.36	2.51
Age (Ma)	5	52	15	117	4	21	13	33	7	22	11
ΣVal. Met. (μg/g)	5	10,211	8307	13,398	4	7196	6645	8303	4703	10,248	6619

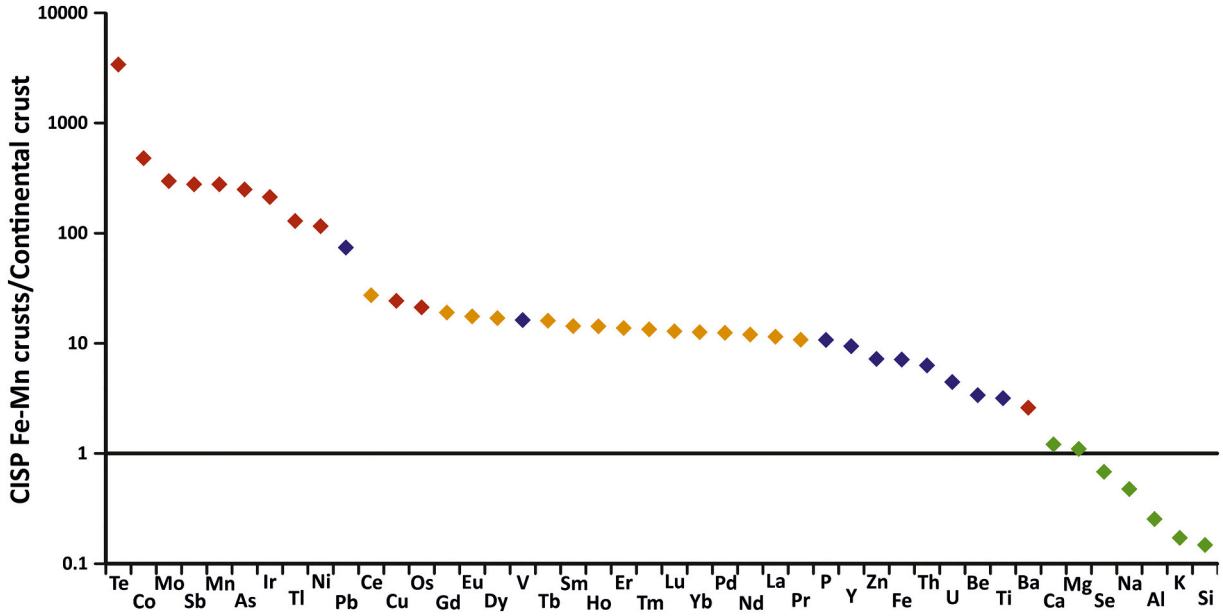

Fig. 5. Element enrichment and depletion diagram of the average CISP Fe—Mn crust content to the composition of the mean continental crust (Rudnick and Gao, 2014); In red are marked the elements associated with Mn, in blue the associated with Fe and in green the silica related elements. REY (orange) can be located between Mn and Fe associations. (For interpretation of the references to colour in this figure legend, the reader is referred to the web version of this article.)

Up to 2200 analyses were made in order to obtain the in-situ geochemistry of the studied samples, differentiating the minerals forming the CISP Fe—Mn crusts. A summary of the obtained results is presented in Table 3. The comparison between the results obtained by the spot mineralogical analysis and Raman microscopy analysis allowed to verify that vernadite shows quite similar contents of Fe and Mn (between 18 and 25 wt%) being characterized by high contents of strategic elements such as Co, Ni, V, Mo, and Ce (0.6, 0.2, 0.13, 0.05 and 0.2 wt%) (Fig. 7F).

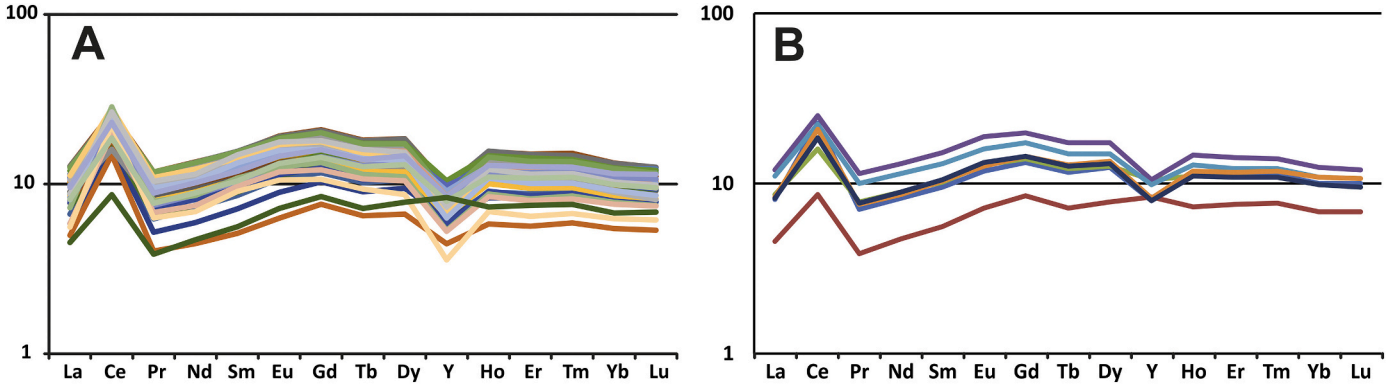

Fig. 6. PAAS (Taylor and McLennan, 1985) normalized bulk REY composition: (A) All studied samples. (B) phosphatized samples.

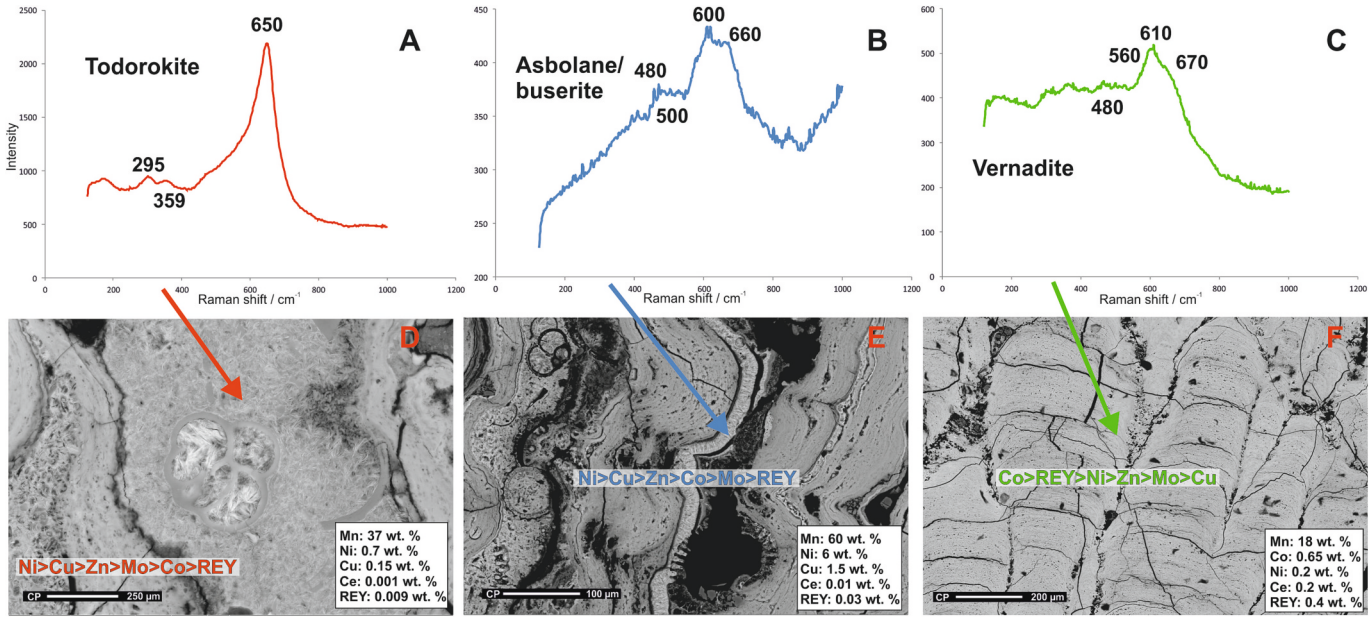

Fig. 7. EPMA phothomicrographs of studied Fe—Mn crusts in which is possible to identify the presence of fibrous minerals (on the left) and the columnar/dense structure (on the right).

On the other hand, asbolane/buserite show higher contents of Mn (up to 45 wt%) and less of Fe (around 5 wt%). These minerals also present high contents of Ni and Cu (respectively in average 2.8, 1.1 wt %), while todorokite show less contents of Mn, Ni and Cu (in average 34 wt% and 6500 and 2000 µg/g respectively) (Fig. 7D, E; Table 3). Asbolane/buserite and todorokite shows low contents of V and Ce on average <500 and 100 µg/g respectively. Manganese minerals exhibit low contents of Si linked elements. In vernadite these elements have an average content of 4 wt% in which Si and Al have the highest values (around 2.8 and 1.2 wt%). Asbolane/buserite, on the other hand, shows slightly higher total contents (in average 7 wt%) but low Si (with minimum under 1 wt%) and high Mg, Na and K contents (respectively 3.5, 1 and 0.7 wt% compared to 1.5, 0.2 and 0.15 present in vernadite). Finally, todorokite has the same Si related elements contents of asbolane/buserite but lower Mg (2.5 vs. 3.5 wt%) and higher Si contents (1,5 vs 0.5 wt%) (Table 3).

Furthermore, through the studied Fe—Mn crusts were analyzed Fe-rich minerals (Fe up to 50 wt%) withlow Mn contents (from 0.5 to 2 wt%) representing essentially goethite group minerals. These minerals are usually impoverished in all trace elements except Cu and V which show average contents of 1200 and 2300 µg/g. In some cases, it is possible to find intermediate minerals with high Fe (up to 40 wt%) and some Mn (4–12 wt%) that also show significant contents of Co, Ni and Ce (in average 4000, 800 and 1000 µg/g) but with less Cu and V (800 and 1000 µg/g respectively). Fe-rich minerals show quite the same Si related elements contents of vernadite with a sum of around 5 wt% and similar distribution with high Si and Al (Supp. Mat. Table 2).

4.6. *Relative REY enrichment in the different minerals*

The use of in-situ analyses with LA-ICP-MS allow to quantify the REY contents in the different minerals recognized in CISP Fe—Mn crusts. These results are summarized in Table 4 and in this section are described from the most enriched to the less. Vernadite and Fe-vernadite show the highest contents of REY reaching a maximum of 4800 µg/g. Ce is the most enriched element with average contents of 2000 µg/g. These results of are coherent with values obtained from bulk analyses (Table 2). The rest of LREEs also show high contents, especially these minerals have high La and Nd (in average 380 and 300 µg/g), followed by Sm and Gd (in average 63 and 62 µg/g respectively) that also are coherent with bulk analyses. HREY have less summary contents from 150 to 450 µg/g represented essentially by Y that can reach 300 µg/g and represent from 9 to 16% of the total REY.

Fe-rich minerals were also analyzed showing that goethite (with Mn

Table 3
EPMA summarized table with the mineralogy of Fe—Mn oxyhydroxides present in all the studied samples distributed for each seamount, N = number of analyses.

Smt.	Echo				The Paps			
Mineral	asbolane/buserite	vernadite	Fe-vernadite	goethite	asbolane/buserite	vernadite	Fe-vernadite	goethite
N	20	84	31	1	87	595	101	10
Mn/Fe	27.88	0.88	0.52	0.02	10.95	0.89	0.53	0.07
Mn (wt%)	34.14	19.50	15.53	1.11	38.22	19.31	15.53	3.01
Fe	1.22	22.21	30.06	46.92	3.49	21.59	29.04	45.03
Si	1.24	1.88	2.34	2.60	0.73	2.15	2.55	3.06
Al	1.02	1.14	1.20	1.94	1.59	1.65	1.71	1.67
Ca	6.25	2.63	2.07	0.50	1.14	2.39	1.95	0.83
K	0.70	0.14	0.11	0.06	0.59	0.19	0.13	0.07
P	0.02	0.15	0.16	0.24	0.06	0.40	0.37	0.38
Co	0.05	0.53	0.44	0.00	0.40	0.61	0.44	0.08
Ni	0.70	0.26	0.19	0.03	2.62	0.32	0.24	0.06
Cu	0.24	0.04	0.04	0.20	0.69	0.07	0.09	0.11
Ce	0.02	0.21	0.23	0.07	0.05	0.24	0.24	0.12
Mg	2.21	1.44	1.45	1.75	3.55	1.36	1.26	1.12
Na	1.08	0.51	0.32	0.29	0.69	0.22	0.19	0.09
Ti	0.07	0.57	0.70	1.13	0.08	0.55	0.55	0.47
V	0.02	0.13	0.17	0.20	0.03	0.13	0.15	0.20
Mo	0.04	0.05	0.04	0.00	0.03	0.05	0.04	0.02
Ba	0.03	0.20	0.25	0.14	0.10	0.16	0.21	0.11
	Drago				Tropic			
	asbolane/buserite	vernadite	Fe-vernadite	goethite	asbolane/buserite	vernadite	Fe-vernadite	goethite
N	0	69	95	15	2	634	104	138
Mn/Fe	–	0.88	0.53	0.26	11.72	0.87	0.46	0.18
Mn (wt%)	–	17.18	13.56	8.56	29.35	19.34	13.49	5.25
Fe	–	19.58	25.40	33.12	2.51	22.11	29.28	29.29
Si	–	2.00	2.51	3.15	0.31	1.73	2.20	2.79
Al	–	1.17	1.26	1.63	2.39	1.22	1.29	2.11
Ca	–	2.37	1.78	1.28	11.02	2.61	1.93	0.91
K	–	0.28	0.11	0.15	0.17	0.15	0.12	0.17
P	–	0.10	0.10	0.17	3.34	0.36	0.41	0.34
Co	–	0.64	0.45	0.28	1.79	0.76	0.55	0.29
Ni	–	0.25	0.16	0.09	2.92	0.28	0.15	0.07
Cu	–	0.03	0.03	0.06	0.36	0.04	0.04	0.06
Ce	–	0.09	0.11	0.10	–	0.20	0.20	0.11
Mg	–	1.51	1.15	1.41	3.98	1.34	1.17	1.48
Na	–	1.39	0.54	0.41	1.94	0.39	0.30	0.17
Ti	–	0.96	1.37	0.77	–	0.56	0.54	1.55
V	–	0.08	0.09	0.10	0.02	0.14	0.18	0.16
Mo	–	0.04	0.02	0.01	–	0.07	0.06	0.03
Ba	–	0.11	0.12	0.11	–	0.15	0.17	0.09

contents below 2 wt%; Supp. Mat. Table 2) display less contents of REY between 350 and 800 μg/g, dominated by Ce as the richest element of the list (from 130 to 400 μg/g). These Fe-oxyhydroxides have a higher proportion of HREY than of LREE with respect to vernadite, with contents from 60 to 140 μg/g, representing 9 to 30% of the total REY content.

Finally, Mn-rich minerals (asbolane/buserite and todorokite) exhibit the lowest REY contents of the studied minerals. Purely Mn-rich minerals have REY contents from 60 to 200 μg/g on the other hand, minerals with slightly high Fe content (from 4 to 10 wt%) show slightly high contents of REY from 200 to 500 μg/g. HREY contents are also low in both types of minerals (respectively from 4 to 20 μg/g and from 20 to 35 μg/g) with HREY% in the same range of vernadite from 5 to 10%. Furthermore, the minerals recognized as Ca-rich todorokite also have low REY contents (ranging 70–110 μg/g), but with high HREY contents in proportion (HREY% from 20 to 34%).

4.7. Growth rates and ages

The calculation of growth rates (GR) was made using data from bulk geochemistry with the empirical equation. The results of the calculation are expressed in Table 2 and graphical representations of growth rates throughout crust sections of Tropic, Drago and The Paps seamounts are showed in Fig. 8. Bulk CISP Fe—Mn crusts show growth rates varying between 0.8 and 2.6 mm/Ma in the biggest seamounts (e.g. The Paps, Tropic, Bimbache) and slightly higher (3.4–4 mm/Ma) in the deepest and smallest seamounts (Gaire and Las Hijas) reaching the highest values in the Amuley sample, 10.2 mm/Ma, due to its high detrital contents (up to 16 wt% for the total Si related elements, Table 2). On the other hand, growth rates calculated in fibrous high-reflective minerals (asbolane, todorokite) can reach up to 100 mm/Ma.

The calculated age depends on the obtained growth rates and the average thickness of the studied crusts. Results vary from 7 to 117 Ma. Between the biggest seamounts, Echo shows the younger ages with an average of 20 Ma and maximum ages of 30 Ma and an average thickness of 33 mm, followed by The Paps with average age and thickness respectively of 33 Ma and 47 mm (Table 2). The oldest crusts can be found on Drago and Tropic Seamounts with average ages of 42 and 52 Ma and thickness of 61 and 72 mm respectively. On the other hand, deeper seamounts like Gaire and Amuley even if show crusts with great thickness (77 and 68 mm) result with younger ages of 21 and 7 Ma respectively (Table 2).

4.8. Statistical analyses

Geochemical data of studied Fe—Mn crusts have been used to create a Pearson correlation matrix and principal component analyses (PCA).

Results of the Pearson correlation matrix are shown in the Supp. Mat. Table 1 identifying the correlation between all elements. Fe and Mn exhibit a strong positive correlation with Co, Ni, Cu, Mo, V, Te and all

Table 4
LA-ICP-MS data obtained by point analyses on the different laminae in selected samples. Results are compiled by genetic process type., N = number of analyses.

Element	Vernadite/birnessite				Asbolane/todorokite			
	N	Mean	Min	Max	N	Mean	Min	Max
Al (wt%)	22	0.6	0.4	1.2	20	0.7	0.1	2
Ca	22	2.5	0.8	4	20	4.6	0.7	18
Mn	22	18	9.7	27	20	39	20	64
Fe	22	21	14	31	20	2.2	0.3	12
Co (μg/g)	22	5404	870	10,300	20	2403	177	15,500
Ni	22	2979	1460	7170	20	22,833	5470	65,100
Cu	22	869	154	3130	20	6867	1340	21,000
Mo	22	535	180	1010	20	498	227	755
Te	22	71	1.08	103	20	4.59	0.01	16.1
La	22	349	106	517	20	25.2	10.7	56.6
Ce	22	1667	591	2340	20	96.5	10.5	273
Pr	22	75.6	23.3	118	20	6.5	2.15	19.3
Nd	22	308	98.8	476	20	27.1	9.91	59.5
Sm	22	63.1	21.1	97.3	20	6.3	2.16	11.5
Eu	22	14.6	4.96	23.5	20	1.5	0.4	3.12
Gd	22	62.2	23.4	90.9	20	6.3	2	14.7
Tb	22	9.01	3.34	14	20	0.9	0.25	2.08
Dy	22	54.3	20.8	83.2	20	5.	1.58	13
Y	22	181	82	269	20	21.8	5.13	55.7
Ho	22	10	4.4	14.2	20	1.13	0.32	2.9
Er	22	28.2	13	41.4	20	3	0.87	7.06
Tm	22	3.8	1.8	5.37	20	0.5	0.12	1.4
Yb	22	24.1	10.8	36	20	2.8	0.9	7.7
Lu	22	3.5	1.6	5.05	20	0.4	0.1	1.1
ΣREY	21	2906	1599	4698	21	262	62	1010

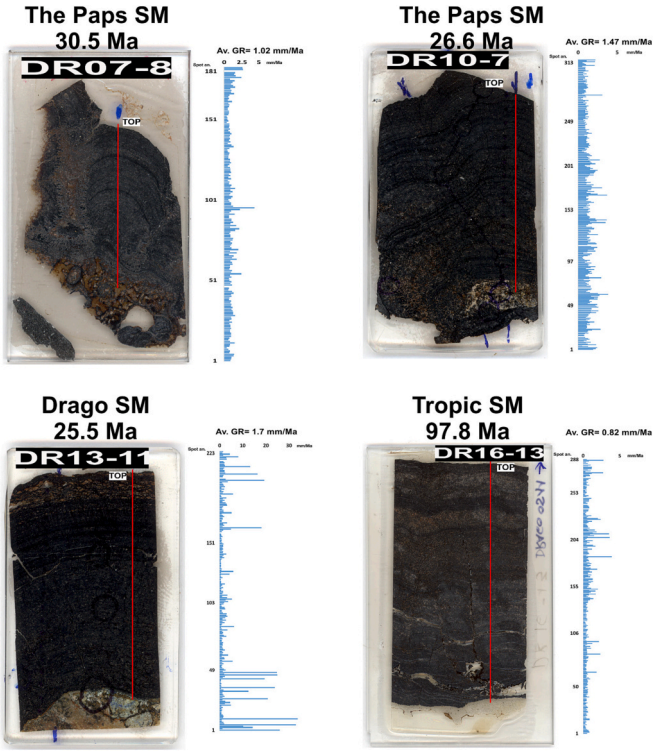

Fig. 8. Growth rates and ages obtained with spot-by-spot analyses made with EPMA in different thin section samples from three seamounts from CISP area. On the right side of each sample is possible to see the average growth rate (Av. GR) and its variation along the studied transect (Modified from Marino et al., 2017, 2018 and Marino, 2020).

REY (between 0.6 and 0.86). On the other hand, Fe and Mn show a negative correlation (reaching −0.6 with Si) with Si related elements. These last only show a positive correlation between each other and with Cu while having negative correlation with the strategic/critical elements and REY (up to −0.6 with Si and Al). Strategic and critical trace elements (Co, V, Mo, Sb, Ba, Te, Tl) have a positive correlation between each other and with all REY between 0.4 and 0.94, with the highest correlation (0.94) represented by Co and Te. Finally, REY exhibit a positive correlation between each other and the strategic/critical elements but a negative correlation with Si related elements and Cu. Considering water depth, all elements show a negative correlation except aluminosilicates and Cu, which show no real correlation and Cu that show a slight positive correlation (+0.4).

PCA shows four components and the projection of data on a binary diagram is useful to evidence the relationship between all the elements and the minerals present in the studied samples. In this way it is possible to highlight all elements linked to Fe and Mn but also the Si related elements and the relationship with CFA separated from the others (Fig. 9). The diagram represents the projection of the different elements by the principal components, in this way in blue and red the Fe—Mn oxyhydroxides and their related elements, in the middle of them is possible highlight (in black) the elements related to Fe-vernadite, in green the elements related the CFA and in yellow siliciclastic elements directly linked with depth.

5. Discussion

In this section the REY contents of CISP crusts will be compared with similar deposits from the world oceans, focusing on the bulk and high-resolution data. In addition, it is considered the dependence of REY to the genetic processes, geographic location and depth. Finally, an economic case of study is presented reporting data on the possible recovery of interesting metals in CISP seamounts.

5.1. REY concentration of CISP crusts compared with other similar deposits

CISP Fe—Mn crusts are composed of low crystalline minerals, essentially Fe-vernadite as the main mineral (>70%) with less birnessite and goethite. Vernadite was also recognized with Raman and the geochemical high-resolution geochemical analyses with EPMA and LA-ICP-MS confirm that is the Mn-mineral which concentrate the highest REY contents in the studied samples (up to 3600 μg/g; Tables 3 and 4). Minor minerals are represented by detrital quartz or calcite (bioclasts) or

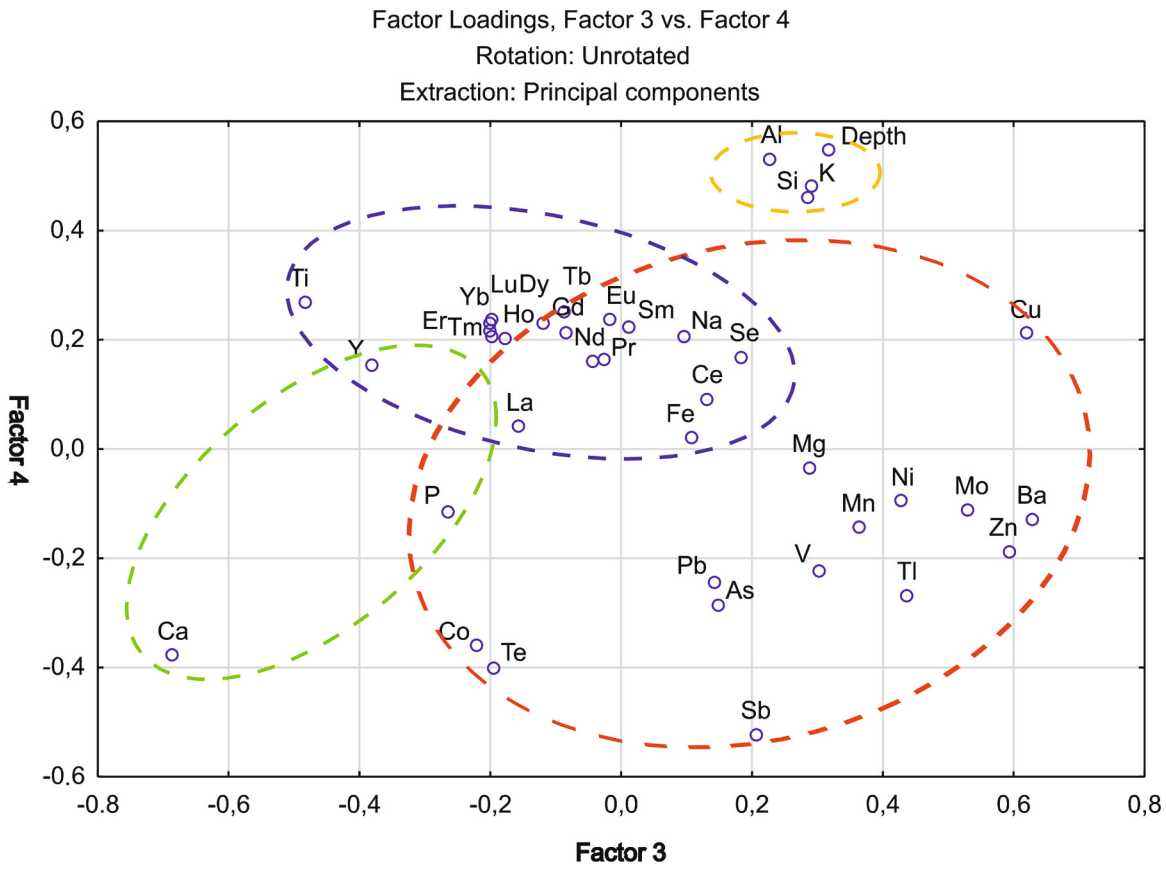

Fig. 9. Principal components diagram. Discontinue areas comprehend elements associated to the different phases: Fe oxyhydroxides (blue), Mn oxides (red), Fe-vernadite (black), CFA (green) and Si related elements (yellow). (For interpretation of the references to colour in this figure legend, the reader is referred to the web version of this article.)

authigenic minerals like CFA or clays (the latter could be formed by the alteration of the basaltic substrate). These minerals are formed by the slow accretion of thin laminae (<20 μ; Figs. 3 and 7) packed in two main structures dense/columnar and dendritic/mottled that reflect both the environmental factor during their formation (i.e. currents) and the genetic process and growth rates. Also observed in other Fe—Mn deposits (Varentsov et al., 1991; Hein et al., 2000; Wang et al., 2011; Muiños et al., 2013; Marino et al., 2017, 2018) (Fig. 3A, Table 2). Similar mineralogy and structures have been also found in several other parts of the Atlantic Ocean with similar REY contents (Cronan, 1975; Koschinsky et al., 1996; Canet et al., 2008; Muiños et al., 2008, 2013; González et al., 2016; Benites et al., 2021, 2023). On the other hand, even if internal structure and mineralogy is similar, samples from the Pacific and Indian oceans show less REY contents as discussed in previous works (Halbach et al., 1981; Bogdanov et al., 1990, 1995; Hein et al., 1997, 2000; Banakar et al., 1997, 2007; Banakar and Hein, 2000; Hein and Koschinsky, 2014; Rajani et al., 2005; Bogdanova et al., 2008; Bau and Koschinsky, 2009; Baturin et al., 2012; Marino et al., 2017, 2019). This mineralogical composition is reflected by the geochemical composition (Table 2). Vernadite together with REY also incorporate in their structure several strategic and critical elements such as Co, Ni, Cu, V, Mo that as can be seen in the Pearson matrix are positively correlated with all REY elements (Tables 3 and 4, Supp. Mat Table 1). In bulk mineralogical analyses, together with the previous minerals listed, it is possible to recognize some small peaks around 10 Å that are related to Mn minerals like asbolane, buserite or todorokite. The presence of these minerals was already described in ferromanganese nodules or crusts from the Pacific and Atlantic oceans, showing a similar internal structure and geochemistry to the CISP Fe—Mn crusts (Hein et al., 2000, 2008; Muiños et al., 2013; Wegorzewski and Kuhn, 2014; Kuhn et al., 2017; Zawadzki et al., 2021).

The presence of ~10 Å minerals is difficult to confirm in bulk XRD due to their small amount in the studied samples. Still, their study was possible using point XRD and Raman analyses and geochemical analyses made with EPMA and LA-ICP-MS (Fig. 7) (Marino et al., 2019). The different minerals present in the studied crusts also affect the contents of REY and other critical elements like Co, Ni, Mo, and V. In this way, samples with the presence of ~10 Å Mn oxides show in bulk with less contents of REY when compared with samples with only vernadite as the Mn mineral phase (in average 2900 compared to 3300 μg/g; Supp. Mat. Table 1). If it is considered other critical elements, samples with asbolane, buserite or todorokite show higher contents of Ni and Cu when compared with samples composed only by vernadite (respectively in average 2800 and 850 μg/g compared to 2300 and 600 μg/g). On the other hand, these samples show less contents of other elements such as Co, V, Mo and Te (in average 3500, 830, 370 and 29 μg/g compared to 5200, 1000, 490 and 45 μg/g). Similar results were also found in Fe—Mn nodules from the Clarion-Clippertone Zone (CCZ) and crusts from Cocos-Nazca Ridge in the Pacific Ocean (Wegorzewski and Kuhn, 2014; Wegorzewski et al., 2015; Hein et al., 2015; Zawadzki et al., 2021). The geochemical differences depend essentially on the presence of these ~10 Å minerals. Spot analyses obtained by EPMA and LA-ICP-MS, show that these minerals have the lowest contents of REY (in average 262 μg/g with a maximum of 1010 μg/g; Table 4). The contents of Mn, Ni and Cu in these minerals are high (on average of 38, 3 and 0.7 wt%, respectively) if compared with vernadite (respectively 19, 0.3 and 0.07 wt%) while the contents of several strategic elements such as Co, V, Te, Nb and Zr (respectively 2400, 300, 5, 9.6 and 49 μg/g) are depleted in these minerals. Similar minerals and geochemistry were also identified in nodules from the CCZ (Wegorzewski and Kuhn, 2014; Wegorzewski et al., 2015; Kuhn et al., 2017).

The Pearson correlation done with bulk data also reflects the dependence of the geochemistry from the mineralogy. First of all, Si related elements show a poor correlation (−0.2 to −0,60; Supp. Mat. Table 1) with all the strategic elements and especially REY that confirm their origin as detrital input from the Canary Islands or sand dusts of the Sahara Desert (Lázaro et al., 2008; Muhs et al., 2010). It is also possible to see that REY elements are clearly linked to Fe an Mn (+0.4 to +0.86) and other elements enriched in vernadite minerals such as Co, Mo, V and Te (between +0.39 and +0.76). 10 Å Mn minerals are usually enriched in Ni and Cu (Tables 2 and 3) and these elements show different correlations with REY. Ni is an element also partially enriched in vernadite minerals so its correlation with REY is not clearly correlated (from 0 to +0.3). Cu, on the other hand, shows a slow negative correlation (−0.3 to −0.42). All these data confirm the dependence of REY on the mineralogy and the genetic process.

5.2. REY dependence on the genetic processes

The presence of a particular genetic process in forming the Fe—Mn crusts can affect the REY contents in different ways. The comparison of bulk geochemistry with spot analyses is represented in Fig. 10. In the ternary diagram are plotted the Fe, Mn and (Co + Ni + Cu)x10 values on the ternary diagram of Bonatti et al., 1972 and modified by Kuhn et al., 2017 and Josso et al., 2017 and in the binary diagram from Dymond et al., 1984. In the bulk diagram are also plotted data of Fe—Mn crusts from other ocean basins (Fig. 10A and B). The result obtained confirmed the diagenetic influence on the formation of selected laminae that is mainly masked in bulk data with a general hydrogenetic growth.

5.2.1. Hydrogenesis

As was mentioned before, the main mineralogy of Fe—Mn crusts is vernadite, formed by the accumulation of nanometric colloids of Fe and Mn s from cold seawaters, a process typical of hydrogenetic growth (Hein et al., 1992, 2000; Koschinsky et al., 1995; Mohwinkel et al., 2014; Usui et al., 2017; Marino et al., 2017, 2019). The colloidal Mn oxide surfaces in the water column provide several free negative charges on which elements dissolved in seawaters could be absorbed. The presence of these charges depends on the mineral structure (phillomanganate), the low crystallinity of these minerals and the formation of vacancies or structural deformations that have to be compensated by

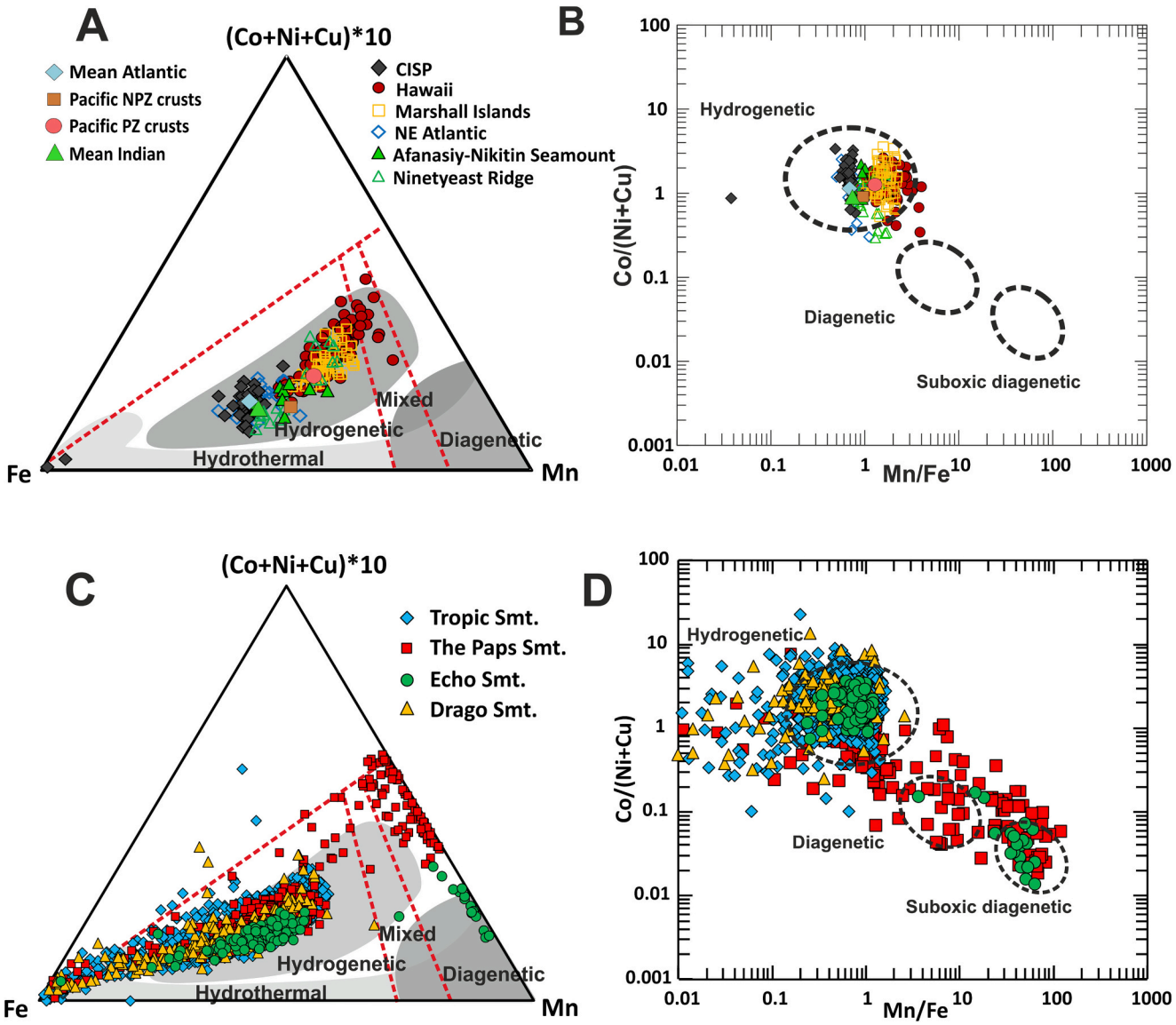

Fig. 10. (A-B) Bulk analyses of studied samples plotted in the modified ternary diagram (Bonatti et al., 1972; Kuhn et al., 2017; Josso et al., 2017) and the binary diagram (Dymond et al., 1984) and compared with samples from other oceans (Hein et al., 2000). (C—D) EPMA spots analysis of samples from four of the different seamounts studied plotted in the ternary and binary diagrams to differentiate genetic processes in the formation of the Fe—Mn oxides.

the absorption of different cations (Manceau et al., 1992a; Post, 1999). The enrichment of hydrogenetic Fe—Mn minerals in similar deposits was also confirmed by previous studies and several authors both for the Atlantic Ocean and the Pacific (Hein et al., 2013, 2016; Muiños et al., 2013; González et al., 2016; Marino et al., 2017, 2019; Kfouri et al., 2021; Benites et al., 2023). The results from layer-by-layer analyses show that vernadite has high contents of REY (sum ranging from 1600 and 4700 μg/g) and when compared with PAAS show a typical positive Ce anomaly and negative Y anomaly (Bau et al., 2014; Hein et al., 2000; Bau et al., 2014; Usui et al., 2017).

Another factor influencing the enrichment in strategic elements and REY of hydrogenetic Fe—Mn minerals is their growth rates. Several researches show that Fe—Mn minerals have different growth rates depending on their genetic process, 0.5–10 mm/Ma for hydrogenetic growth, 10–100 mm/Ma for diagenetic and 100–1000 mm/Ma or more for hydrothermal minerals (Hein et al., 1997, 2000). The slow growth rates typical of hydrogenetic minerals allow the absorption of dissolved REY found in the marine environment as mono- and di- carbonates, on the structure of the recently precipitated oxyhydroxide colloids (Bau, 1996; Byrne and Sholkovitz, 1996; Bau et al., 2014; Baturin et al., 2012). Calculated growth rates with bulk data of the Fe—Mn crusts of the different CISP seamounts are in the range attributed to hydrogenetic processes but Amuley samples show growth rates more typical of diagenetic formation (10.18 mm/Ma). These calculated high growth rates could also be due to the high contents of aluminosilicates (in total 17 wt%) with detrital origin transported by bottom currents at the base of the seamount that dilute the contents of Fe, Mn and Co contents and increase the sedimentation rate (Table 1).

5.2.2. *Diagenesis*

The presence of 10 Å Mn minerals in CISP Fe—Mn crusts has been proved by the use of high resolution mineralogical and geochemical analyses. These minerals show different elemental contents if compared with vernadite, essentially in their high contents of Mn, Ni and Cu and low contents of several strategic elements (such as Co, V and REY) (Tables 3 and 4). All these differences are linked to the genetic process acting during their formation. Asbolane, buserite and todorokite are minerals usually linked to the diagenetic process of pore water precipitation or dissolution and precipitation of previous formed Fe—Mn oxyhydroxides in diagenetic conditions (Hein et al., 2000, 2013, 2016; Mohwinkel et al., 2014; Kuhn et al., 2017). The Mn/Fe ratio of these laminae is high (> 10) typical of early stage of diagenesis either under oxic or suboxic conditions (Halbach et al., 1988; Wegorzewski and Kuhn, 2014; Marino et al., 2018, 2019; Kfouri et al., 2021; Zawadzki et al., 2021). The comparison of REY contents of these minerals with PAAS (Fig. 11) show a different pattern when compared with that obtained for vernadite. Asbolane, buserite and todorokite show none or negative Ce anomalies that when intermixed with vernadite change to a small positive anomaly (Fig, 11 A and B). Similar patterns have been also seen in thin diagenetic samples from Cocos-Nazca Ridge (Zawadzki et al., 2021). In general, all these laminae have no or small negative Y anomaly. Finally, it is possible to identify the presence of some laminae with an intermediate behavior (Fig. 11) both, due to mixed diagenetic laminae or to Fe-rich laminae with hydrogenetic signature with intermediate REY contents. Enrichment of REY in freshly precipitated Fe-oxyhydroxides have been also found in land waters (Santofimia et al., 2022). All these data confirm the diagenetic origin of these minerals, as could also be seen in other studies of similar deposits (Bau et al., 2014; Kuhn et al., 2017). These minerals also show a different structure when compared with hydrogenetic minerals. Asbolane and buserite are both phyllomanganates but with different structure. The former form a structure with octahedral sheets of MnO_6 separated by a layer of metal octahedrons cations formed by hydroxyl metals that are connected with the Mn sheets by the link of H bonds r and the O from the Mn layer. The metal layer is usually formed by Li, Co, Ni and other transitional metals (Manceau et al., 1992a, 1992b, 1997; Post, 1999). Buserite is considered a precursor of the birnessite with a 10 Å interlayer of water that could be stabilized by the incorporation of big cations in the interlayer (Mg, Ca, Co, Ni) (Manceau et al., 1992a, 1992b, 1997; Post, 1999). Todorokite, on the other hand, show a tunnel structure formed by 3 × 3 octahedron chains that share corners in order to form a stable structure that did not collapse after drying and allow incorporate several big cations in the tunnels (e.g. Mg, Na, Ca, K, Ni, Cu, etc.) (Manceau et al., 1992a, 1992b; Post, 1999). The presence of all these big cations, both stabilizing buserite and asbolane structure or included in the tunnel structure of the todorokite can be confirmed by point analyses (Tables 3 and 4). The structure of these minerals, stabilized essentially by Ni, Cu and Mg cations, show less free charges on which dissolved mono- and di-carbonates could be absorbed.

Together with the differences in structure and cations sorption, growth rates also influence the incorporation of metals. As was seen before, diagenetic minerals are usually formed at growth rates of 10–100 mm/Ma. High-resolution analyses made on selected diagenetic minerals in studied samples allowed the estimation of their growth rates within a range varying between 11 and 300 mm/Ma (Supp. Table 2). These high growth rates did not allow the incorporation of dissolved metals from seawater making diagenetic minerals depleted in several strategic elements and especially REY (Table 4).

5.2.3. *Phosphatization*

Phosphatization is a process similar to diagenesis in which previously formed minerals (essentially carbonate and Fe—Mn oxyhydroxides) are substituted by phosphates in the marine environment when fluids are enriched in dissolved phosphorous and the redox condition are favorable (Hein et al., 1997, 2000, 2016; Koschinsky et al., 1997).

Phosphates minerals concentrate in their structure some contents of different heavy REE and especially Y that could increase the REY contents of the studied Fe—Mn crusts. CISP Fe—Mn crusts with P contents high enough to consider the presence of phophatization show similar REY contents to those of from non-phosphatized crusts and their representation compared with PAAS also reflect a pattern comparable to the

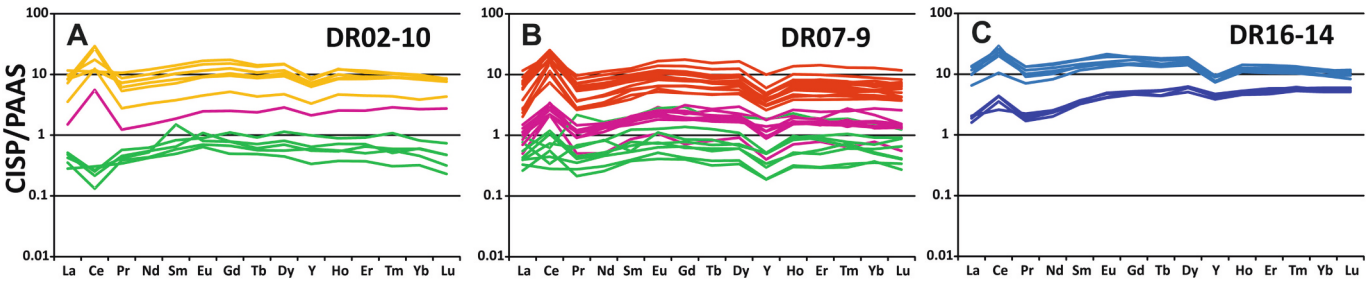

Fig. 11. REY diagram obtained with punctual analysis with LA-ICP-MS on selected samples. A and B) In green diagenetic laminae, in violet mixed laminae for samples DR02–10 and DR07–9. C). In dark blue Fe rich laminae of sample DR16–14. (For interpretation of the references to colour in this figure legend, the reader is referred to the web version of this article.)

other studied Fe—Mn crusts (Fig. 5). The only sample with a different behavior is DR07–8 that together with high P contents also showed the presence of diagenetic minerals (Fig. 5, Table 2) but, unlike the others crusts with diagenetic influence, it presents a positive Y anomaly (Fig. 5). High-resolution spot analyses made on similar diagenetic minerals in crusts DR02–10 and DR07–9 did not show enrichment of Y. Conversely, results of the analyses on these minerals have 10 times less Y contents with respect to hydrogenetic ones (Table 4). Furthermore, the result of the sequential leaching of this crust shows that the Y sum of the four fractions (calcite, Mn-oxides, Fe-oxyhydroxides, residuals) (109 μg/g) only corresponds to half of the total Y (225 μg/g). In contrast, in the other analyzed crust (DR16–13), the sum of the four fractions is 70% of the total. This difference could be due to the presence of some phosphates minerals that cannot be dissolved in the fourth fraction (Marino et al., 2018, 2019).

In any case, the actual data obtained on CISP Fe—Mn crusts are insufficient to demonstrate that the presence of phospatization may entail an enrichment of REY in Fe—Mn crusts. Further studies involving Fe—Mn crusts, nodules and phosphorites recovered in Tropic Seamount may help to elucidate the role of phosphatization on the composition of Fe—Mn crusts.

5.3. Controls of REY related with depth and location

Many elements that compose Fe—Mn oxyhydroxides as the main elements Fe and Mn, together with Co, Ni, Mo, V and Pb amongst others are enriched in the OMZ in their reduced form (Johnson et al., 1996; Saager et al., 1997; Hein et al., 2000; Milne et al., 2010; Pohl et al., 2011). As can be observed by results from other studies on Fe—Mn crusts with hydrogenetic origin, which main mineral is vernadite, show a high scavenging of REY elements in the solid phase vs seawater (Bau, 1996; Bau et al., 2014). Therefore, Fe—Mn crusts formed within the OMZ or at depths just below, that also show slow growth rates, should be enriched in these elements. Moreover, seawater within or proximal to the OMZ is enriched in dissolved REY owing to the desorption of these elements due to the local reductive dissolution of Fe—Mn oxides and subsequent precipitation in moments of oxidation due to the mixing of water masses (e.g. De Baar et al., 1988; Sholkovitz et al., 1992; Schijf et al., 1995).

Despite the fact that samples from the west part of The Paps seamount show a slightly high presence of diagenetic minerals, the depth and position for the occurrence of Fe—Mn crusts on the seamounts seem to not have any influence on their mineralogy. The presence of diagenetic minerals on the western side of this seamount is probably linked to the fall of detritus and sands from the top of the seamount. These detrital minerals are also clearly visible in EPMA images and have been associated to the presence of bright fibrous diagenetic laminae, this detrital enrichment could be due to the presence of landslides visible in in the bathymetry (Palomino et al., 2016; Marino et al., 2019).

In order to test the possible controls of REY contents associated with depth and location in studied Fe—Mn crusts, only hydrogenetic samples from the same seamount have been taken into account. Samples from the Paps Seamount show the highest variability of depths useful to see if there is a direct connection with REY contents. Results show that when the depth increases, the REY contents decrease progressively (Fig. 12, Supp. Mat. Table 1). Samples collected at depths around 1800 m are the most enriched with up to 3800 μg/g followed by samples with depths around 2300 m with up to 3400 μg/g located on the west side. Finally, samples from the deepest part of the seamount (around 2900 m) located

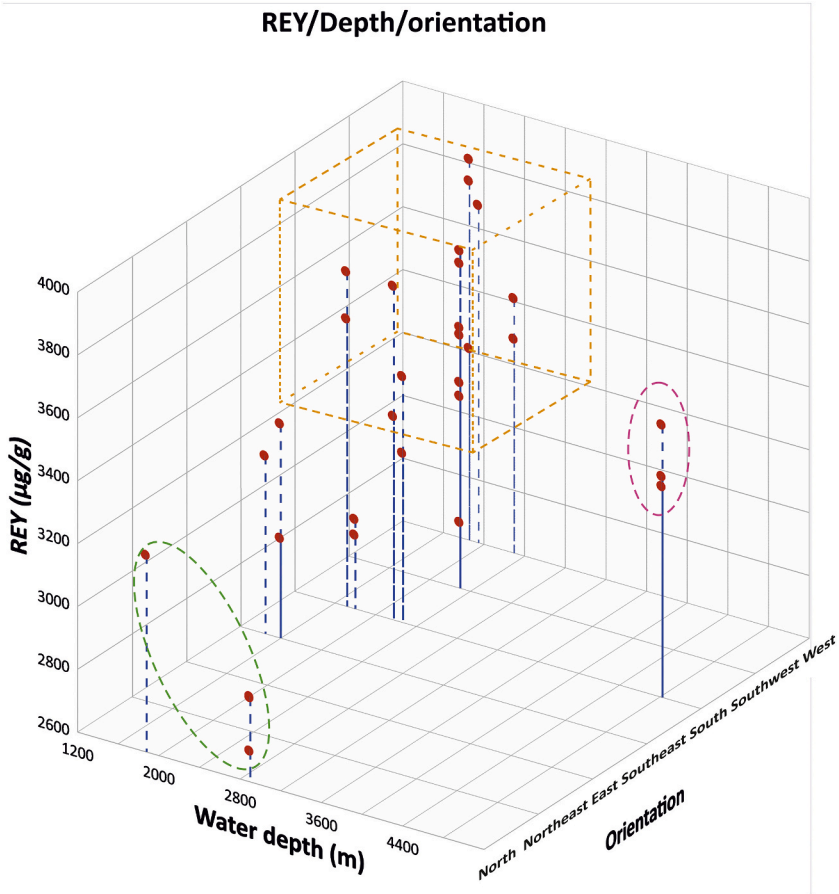

Fig. 12. Comparison of depth, orientation and REY contents of the purely hydrogenetic samples. In the yellow cube are located the shallowest samples with high REY contents, in the green area the deeper samples faced to north with low REY and in yellow area deepest samples faced to south that instead show high REY contents. (For interpretation of the references to colour in this figure legend, the reader is referred to the web version of this article.)

on the north-west side of the seamount show the lowest REY contents with maximums of 2870 μg/g (Fig. 11, Supp. Mat. Table). Mineralogical data of these samples confirm the presence of only hydrogenetic minerals as vernadite with less goethite and the geochemical data also show that there is no dilution due to the presence of detrital elements (Si, Al, Ca) from the top that could explain the lower REY contents. In this way the only controls that could affect REY contents are those associated to depth and position of the sample in the seamount.

Deeper samples are located almost 1000 m below the lower part of the OMZ (whose core is located between water depths of 400 and 700 m) and that could extend down to 1700 m deep (Brandt et al., 2010, 2012; Marino et al., 2017). At these depths seamount slopes are bated by the deepest currents, from the north the North Atlantic Deep Water (NADW) and from the south by the Antarctic Intermediate Water (AAIW) and the Antarctic Bottom Water (AABW). The first two currents have different characteristics, but essentially different dissolved oxygen (DO), the NADW showing the highest DO around 200 μmol/kg, that is double with respect to the AAIW that shows 110 μmol/kg (Mémery et al., 2000; Bashmachnikov et al., 2015). On the other hand, studies made on several water samples demonstrated that AABW have high contents of dissolver REY compared with the other water masses (German et al., 1995). These differences in DO could and REY contents together with redox interaction caused by the mixing of waters also affect the concentration of the elements in samples exposed to them. The comparison of samples with almost the same depth (2180 and 23,000 m) but recovered in different part of the seamount show that samples from the south have a slightly higher REY contents than those recovered on the west-north slope (maximum of 3700 μg/g compared with 3400 μg/g) due to the action of the AAIW. Also, deepest samples (4800 m) recovered from southern part of the Gaire Seamount show similar REY contents to those that are located within or just below the OMZ (DA06–1, DA06–2 and DA06–7) (Fig. 12, Supp. Mat. Table 1). This is also supported by the principal component analysis (Fig. 8) in which is possible to see that the depth is only related with Si related elements, while REY are related with Mn and Fe oxyhydroxides.

Finally, we compare spot data obtained with LA-ICP-MS from the top of samples with different orientations, sample DR16–14 in the Tropic seamount oriented south and DR02–10 in the Echo seamount oriented north and both at similar depths around 1800 m. Point data show that in Tropic sample the uppermost layers have high REY contents (up to 3800 μg/g in hydrogenetic Fe—Mn laminae and 3700 μg/g in Fe-rich laminae), while data obtained on sample from the Echo show less REY contents between 2000 and 2700 μg/g (Supp. Mat. Table 2). Also, if considering bulk data, the deepest samples (4800 m) recovered from southern part of the Gaire seamount show similar REY contents to those located within or just below the OMZ (DA06–1, DA06–2 and DA06–7) (Fig. 12, Supp. Mat. Table 1). These results show that the exposition to different deep currents (NADW from the north and AAIW from the south) could influence the enrichment of REY in the different samples. It also confirms the influence of the different currents NADW and AAIW on the forming Fe—Mn samples.

In summary, the contents of REY are strictly linked to the mineralogy, orientation and depth of the samples. Samples with the presence of diagenetic minerals (asbolane, buserite, todorokite) show low bulk contents of REY if compared with samples purely hydrogenetic (eg. DR07–0 and DR07–9 compared to DR0710; Supp. Mat. Table 1). The orientation of Fe—Mn crusts and their exposure to different deep currents also have an influence on the REY contents. Samples located on the northern side of the seamounts and exposed to the NADW show lower REY contents than those located on the south (or south-west) with major exposition to the AAIW and AABW (Fig. 12, Supp. Mat. Table 1). This difference mainly depends on the DO contents of the seawater masses that could affect the redox condition locally and promote the dissolution of Fe—Mn crusts and enrichment in several elements and REY. Finally, depth also shows a key behavior in studied Fe—Mn crusts, in this way, shallowest samples (around 1700 m), right below of the OMZ, show the highest contents of REY (up to 3400 μg/g). REY contents start to decrease with greater water depths reaching the minimum at depths around 3000 m (around 2700 μg/g) essentially due to the distance from OMZ as was also observed in Fe—Mn crusts from Rio Grande Rise (Benites et al., 2023).

5.4. Case of study: economic interest of REY in CISP seamounts

REY bulk contents observed in studied Fe—Mn crusts (Table 2) seem high enough to consider its extraction as a by-product of the main metal extraction represented by Mn, Fe, Co, Ni, Cu, and V. Two different extractive experiments have been made on five Fe—Mn crusts showing that both the selective extraction as well as the experiment with the addition of a reducing agent, results in recovery rates for all REY between 70 and 90% (Table 6). In both experiments it is also clear that hydrogenetic Fe—Mn crusts show the highest recovery rates (up to 85%), due to a better digestion of hydrogenetic minerals when compared to diagenetic ones (Marino et al., 2018, 2019).

Data obtained in these samples allow calculating the amount of metal that can be extracted in a possible mining site on the top of the seamounts. In order to make the correct calculation it is important to know the average thickness of the crusts present on the seamount, the average geochemical contents and the recovery rate obtained in samples from the same seamount. The average thickness of the top of the Tropic Seamount has been calculated using data from Yeo et al., 2019 in which several areas of the seamount have been sampled with cores drilled by ROV. The data obtained give an average thickness of 46 mm for the top of the seamount. The average thickness of the crusts from Echo and The Paps seamounts have been calculated using data obtained during the study of the CISP area (Table 1). The density of the Fe—Mn crusts is variable depending on the porosity and the mineralogy of the crusts but has been calculated at an average dry density of 1,3 g/cm^3 based on the study of several samples from the Pacific Ocean (Hein et al., 2009; Hein and Koschinsky, 2014). With these data it is possible to calculate the dry tons of Fe—Mn crusts for each seamount taking into account a surface of 1 Km^2. The value of dry tons for each element has been calculated using the total dry tons and the average wt. percentage calculated in the result chapter (Table 2).

With all these data it was possible to calculate the recovered tons of metals for possible mine sites in the three selected seamounts resumed in Table 5. The most interesting values are represented by the contents of Mn (ranging from 6000 to 9400 tons) and Fe (ranging from 6300 and 9300 tons) but especially by the high amount of strategic elements as Co, Ni and V (265, 92 and 50 tons respectively). REY recovery tonnage is also very high with the maximum values obtained for seamounts in which have been found only purely hydrogenetic samples (160 tons) while in seamount in which there is the presence of mixed samples are slightly low (109 and 126 tons).

REY values will depend essentially on the mineralogy of the samples; samples with higher diagenetic influence as DR07–9 from The Paps Seamount (Marino et al., 2019) show the lowest recovery rates due to the presence of several laminae formed by diagenetic minerals with low contents of REY (from 60 to 270 μg/g). These minerals also show the poorest digestion probably due to their genetic formation and the better-formed crystals. Comparison with the sequential leaching experiment shows that the total recovery rates, by adding the hydroxylamine and hydrochloric acid results, increase about 10 to 20% for several critic elements. In this way better recovery rates have been found, especially for Mn Co and Ni, also in diagenetic-influenced Fe—Mn crusts (Marino et al., 2018). The REY recovery rates also increase a little from 80% to 88% with no distinguishable difference in purely hydrogenetic or mixed diagenetic samples. In this way, REY recovery tonnageons could increase by about a factor of 14% for the diagenetic-influenced crusts and by 7–8% for hydrogenetic sample types.

With these data it is possible to propose an extraction of elements in two phases in order to mine the maximum contents possible for all the

Table 5
Dry Tons contents, recovery rates and recovery Tons of the different valuable metals in a square kilometer of Fe—Mn crusts from CISP seamounts.

		REY	Co	Ni	Cu	V	Mo	Mn	Fe
Echo	Dry Tons	130	208	100	18	43	17	7381	10,855
	Rec. Rates	84	95	85	74	85	63	81	58
	Rec. Tons	109	198	85	13	37	11	5979	6296
The Paps	Dry Tons	170	315	151	39	55	25	10,299	14,539
	Rec. Rates	74	84	53	68	58	26	75	49
	Rec. Tons	126	265	80	27	32	6	7724	7124
Tropic	Dry Tons	197	341	132	24	60	30	11,601	16,266
	Rec. Rates	81	63	70	50	83	42	81	57
	Rec. Tons	160	215	92	12	50	13	9397	9271

interesting metals considering REY not only as by-product but in most cases a primary metal with Co and Ni.

It is important to highlight that before starting any possible future mining, there is the obligation to preserve the marine environment to prevent, reduce and control the possible pollution derived from the mining site. For this reason, EU has drafted the EU Directive 2008/56/EC (European Directive, 2023) to achieve a good environmental status for all the EU's marine waters and protect the different biotas. The seamounts from the Canary Islands area may represent natural laboratories where technological developments and further seabed investigation should be conducted to confirm that these mineral resources can be recovered with minimal environmental impact.

6. Conclusions

In this work a complete set of 42 Fe—Mn crusts from 8 seamounts of the CISP have been analyzed for their contents of REY and their relationship with mineralogy, genetic process, localization and depth.

Fe—Mn crusts concentrate great amounts of REY, but this concentration depends on several factors.

Mineralogy and genetic processes are the main factors controlling REY contents. Due to its structure, Fe-vernadite can concentrate high contents (in average 3000 μg/g with a maximum of 4700 μg/g) of total REY and especially LREY (with the highest contents represented by Ce up to 2300 μg/g). Vernadite formation is linked to the hydrogenetic process and to the slow growth of these minerals (between 0.2 and 2 mm/Ma).

On the other hand, asbolane, buserite and todorokite are the minerals with the lowest REY contents (on average 260 μg/g). This depends on the mineral structure of these that need the presence of big cations as Ni and Cu to be stable (asbolane and buserite) or the tunnel structure of 10 Å that did not allow the entrance of the biggest of -mono and -di carbonate that usually are linked to dissolved REY. Moreover, these minerals are linked to diagenetic processes and fast growth rates with up to 500 mm/Ma.

Another important factor is the formation depth of the samples. Fe—Mn crusts from shallower depth of 1800 m are more enriched in REY (up to 3800 μg/g) due to the presence of the OMZ that promote very slow growth rates and also the possible dissolution of Fe—Mn minerals previously formed that locally enrich seawater of dissolved REY. With depth REY contents slowly decrease reaching contents of 2800 μg/g at 3000 m water depth. Together with depth the location of the samples and the water masses that bated them also influence REY contents. Fe—Mn crusts located in the north face of the seamount show less REY contents due to the high oxygenated waters of the NADW. On the other hand, sample deeper (4800 m) but located on the south part of the seamounts show high REY contents (average of 3300 μg/g) due to the mixing of waters masses represented by the low oxygenated AAIW and the enriched in REY AABW.

Further studies realized with sets of samples collected in situ at different depth of several seamounts together with the use of high-resolution spot-by-spot analyses would help to increase the correlation of the variation of REY in CISP area with local, regional o global oceanic changes.

Finally, the economic case of study made on data obtained on three seamounts of the CISP show that the future possible mine and hydrometallurgical process of recovered Fe—Mn crust could provide in average 130 tons of REY together with other strategic and base metals such as Mn, Fe, Co, Ni, Cu, V and Mo. In this way several studies have to be made in order to evaluate what is the environmental impact of all the processes involved in the exploitation of these deposits.

Supplementary data to this article can be found online at https://doi.org/10.1016/j.margeo.2023.107144.

Declaration of Competing Interest

The authors declare the following financial interests/personal relationships which may be considered as potential competing interests:

Egidio Marino reports financial support was provided by European Commission. Egidio Marino reports financial support was provided by State Agency of Research. Catarina Miguel reports financial support was provided by Fundação para a Ciência e a Tecnologia (FCT).

Data availability

The authors declare that the data supporting the findings of this study are available within the paper and its supplementary information files.

Acknowledgements

This research is funded by the ATLANTIS project (PID2021-124553OB-I00) of the Spanish State Investigation Agency (AEI), European contract EMODnet-Geology (EASME/EMFF/2016/1.31.2-Lot 1/SI2.750862), and the Horizon Europe projects GSEU (HORIZON-CL5-2021-D3-02-14, Project 101075609) and TRIDENT (Grant agreement ID: 101091959). Authors would also like to thank all the staff of the General Laboratories of the Geological and Mining Institute of Spain (IGME-CSIC) for their help in obtaining the different results. Raman analysis were supported by Portuguese national funds through the FCT—Fundação para a Ciência e a Tecnologia, I.P., within the projects UIDB/04449/2020 and UIDP/04449/2020 (HERCULES Laboratory). C. M. thanks, DL57/2016/CP1372/CT0012 ("Norma Transitória"). We also thanks reviewers and editor for their constructive comments useful to improve the quality of the manuscript.

References

Abed, A.M., Al Kuisi, M., Khair, H.A., 2009. Characterization of the Khamaseen (spring) dust in Jordan. Atmos. Environ. 43, 2868–2876.

Banakar, V.K., Hein, J.R., 2000. Growth response of a deep-water ferromanganese crust to evolution of the Neogene Indian Ocean. Mar. Geol. 162, 529–540. https://doi.org/10.1016/S0025-3227(99)00077-8.

Banakar, V.K., Pattan, J.N., Mudholkar, A.V., 1997. Palaeoceanographic conditions during the formation of a ferromanganese crust from the Afanasiy-Nikitin seamount, North Central Indian Ocean: geochemical evidence. Mar. Geol. 136, 299–315. https://doi.org/10.1016/S0025-3227(96)00065-5.

Banakar, V.K., Hein, J.R., Rajani, R.P., Chodankar, A.R., 2007. Platinum group elements and gold in ferromanganese crusts from Afanasiy-Nikitin seamount, equatorial

Indian Ocean: sources and fractionation. J. Earth Syst. Sci. 116 (1), 3–13. https://doi.org/10.1007/s12040-007-0002-x.
Bashmachnikov, I., Nascimento, Â., Neves, F., Menezes, T., Koldunov, N.V., 2015. Distribution of intermediate water masses in the subtropical Northeast Atlantic. Ocean Sci. 11, 803–827.
Baturin, G.N., Dubinchuk, V.T., Rashidov, V.A., 2012. Ferromanganese crusts from the Sea of Okhotsk. Oceanology 52, 88–100.
Bau, M., 1996. Controls on the fractionation of isovalent trace elements in magmatic and aqueous systems: evidence from Y/Ho, Zr/Hf, and lanthanide tetrad effect. Contrib. Mineral. Petrol. 1996 (123), 323–333.
Bau, M., Koschinsky, A., 2009. Oxidative scavenging of cerium on hydrous Fe oxide: evidence from the distribution of rare earth elements and yttrium between Fe oxides and Mn oxides in hydrogenetic ferromanganese crusts. Geochem. J. 43 (1), 37–47. https://doi.org/10.2343/geochemj.1.0005.
Bau, M., Schmidt, K., Koschinsky, A., Hein, J., Kuhn, T., Usui, A., 2014. Discriminating between different genetic types of marine ferro-manganese crusts and nodules based on rare earth elements and yttrium. Chem. Geol. 381, 1–9.
Benites, M., Hein, J.R., Mizell, K., Jovane, L., 2021. Miocene phosphatization of rocks from the summit of Rio Grande Rise, Southwest Atlantic Ocean. Paleoceanogr. Paleoclimatol. 36 (9) https://doi.org/10.1029/2020PA004197.
Benites, M., González, J., Hein, J., Marino, E., Reyes, J., Millo, C., Jovane, L., 2023. Controls on the chemical composition of ferromanganese crusts from deep-water to the summit of the Rio Grande Rise, South Atlantic Ocean. Mar. Geol. 462, 107094. https://doi.org/10.1016/j.margeo.2023.107094.
Berger, A., Janots, E., Gnos, E., Frei, R., Bernier, F., 2014. Rare earth element mineralogy and geochemistry in a laterite profile from Madagascar. Appl. Geochem. 41, 218–228. https://doi.org/10.1016/j.apgeochem.2013.12.013.
Bogdanov, Y.A., Sorochtin, O.G., Zonenshain, L.P., Kuptzov, V.M., Lisitzina, N.A., Podrajanski, A.M., 1990. Ferromanganese Crust and Nodules of Pacific Seamounts. Nauka, Moscow, Russia, p. 229.
Bogdanov, Y.A., Bogdanova, O.Y., Dubinin, A.V., Gorand, A., Gorshkov, A.I., Gurvich, E. G., Isaeva, A.B., Ivanov, G.V., Jansa, L.F., Monaco, A., 1995. Composition of ferromanganese crusts and nodules at northwest Pacific guyots and geologic and paleoceanographic considerations. In: Haggerty, J.A., Premoli Silva, I., Rack, F.R., McNutt, M.K. (Eds.), Proceedings of the Ocean Drilling Program: Scientific Results, 144. Ocean Drilling Program, College Station, TX, USA, p. 1059.
Bogdanova, O.Y., Gorshkov, A.I., Novikov, G.V., Bogdanov, Y.A., 2008. Mineralogy of morphogenetic types of ferromanganese deposits in the world ocean. Geol. Ore Depos. 2008 (50), 462–469.
Bonatti, E., Kraemer, T., Rydell, H., 1972. Classification and genesis of submarine ironmanganese deposits. In: Horn, D.R. (Ed.), Ferromanganese Deposits of the Ocean Floor. Arden House, New York, pp. 149–165.
Brandt, P., Hormann, V., Körtzinger, A., Visbeck, M., Krahmann, G., Stramma, L., Lumpkin, R., Schmid, C., 2010. Changes in the ventilation of the oxygen minimum zone of the tropical North Atlantic. J. Phys. Oceanogr. 40, 1784–1801. https://doi.org/10.1175/2010JPO4301.1.
Brandt, P., Greatbatch, R.J., Claus, M., Didwischus, S.-H., Hormann, V., Funk, A., Hahn, J., Krahmann, G., Fischer, J., Körtzinger, A., 2012. Ventilation of the equatorial Atlantic by the equatorial deep jets. J. Geophys. Res. Oceans 117, C12015. https://doi.org/10.1029/2012JC008118.
Byrne, R.H., Sholkovitz, E.R., 1996. Marine chemistry and geochemistry of the lanthanides. In: Gschneidner Jr., K.A., Eyring, L. (Eds.), Handbook of the Physics and Chemistry of Rare Earths, vol. 23. Elsevier Science B.V, pp. 497–593.
Canet, C., Prol-Ledesma, R.M., Bandy, W.L., Schaaf, P., Linares, C., Camprubí, A., Tauler, E., Mortera-Gutiérrez, C., 2008. Mineralogical and geochemical constraints on the origin of ferromanganese crusts from the Rivera Plate (western margin of Mexico). Mar. Geol. 251, 47–59. https://doi.org/10.1016/j.margeo.2008.01.012.
Chakhmouradian, A.R., Wall, F., 2012. Rare earth elements: minerals, mines, magnets (and more). Elements 8 (5), 333–340. https://doi.org/10.2113/gselements.8.5.333.
Chao, E.C.T., Back, J.M., Minkin, J.A., Tatsumoto, M., Junwen, W., Conrad, J.E., McKee, E.H., Zonglin, H., Qingrun, M., Shengguang, H., 1997. Sedimentary carbonate-hosted giant Bayan Obo REE-Fe-Nb ore deposit of Inner Mongolia, China; a cornerstone example for giant polymetallic ore deposits of hydrothermal origin. In: U.S. Geological Survey Bulletin, 2143. U.S.G.S publication (65 pp).
Collinet, M., Charlier, B., Namur, O., Oeser, M., Médard, E., Weyer, S., 2017. Crystallization history of enriched shergottites from Fe and Mg isotope fractionation in olivine megacrysts. Geochim. Cosmochim. Acta 207, 277–297. https://doi.org/10.1016/j.gca.2017.03.029.
Cronan, D.S., 1975. Manganese nodules and other ferromanganese oxide deposits from the Atlantic Ocean. J. Geophys. Res. 80 (27), 3831–3837.
De Baar, H.J., German, C.R., Elderfield, H., van Gaans, P., 1988. Rare earth element distributions in anoxic waters of the Cariaco Trench. Geochim. Cosmochim. Acta 52 (5), 1203–1219. https://doi.org/10.1016/0016-7037(88)90275-x.
Deady, É.A., Mouchos, E., Goodenough, K., Williamson, B.J., Wall, F., 2016. A review of the potential for rare-earth element resources from European red muds: examples from Seydişehir, Turkey and Parnassus-Giona, Greece. Mineral. Mag. 80 (1), 43–61. https://doi.org/10.1180/minmag.2016.080.052.
Dostal, J., 2016. Rare metal deposits associated with alkaline/peralkaline igneous rocks. In: Verplanck, P., Hitzman, M. (Eds.), Rare Earth and Critical Elements in Ore Deposits. Society of Economic Geologists, Littleton Colorado, pp. 33–54. https://doi.org/10.5382/Rev.18.02.
Drew, L., Qingrun, J., Weijun, S.M., 1990. The Bayan Obo iron-rare-earth-niobium deposits, Inner Mongolia, China. Lithos 26, 43–65. https://doi.org/10.1016/0024-4937(90)90040-8.
Dubinin, A.V., 2004. Geochemistry of rare earth elements in the Ocean. Lithol. Miner. Resour. 39 (4), 289–307. https://doi.org/10.1023/B:LIMI.0000033816.14825.a2.
Dubinin, A.V., Rozanov, A.G., 2001. Geochemistry of rare earth elements and thorium in sediments and ferromanganese nodules of the Atlantic Ocean. Lithol. Miner. Resour. 36 (3), 268–279. https://doi.org/10.1023/A:1010485510346.
Dymond, J., Lyle, M., Finney, B., Piper, D.Z., Murphy, K., Conard, R., Pisias, N., 1984. Ferromanganese nodules from MANOP Sites H, S, and R—Control of mineralogical and chemical composition by multiple accretionary processes. Geochim. Cosmochim. Acta 48, 931–949. https://doi.org/10.1016/0016-7037(84)90186-8.
European Directive, . 2008/56/EC of the European Parliament and of the Council of 17 June 2008 establishing a framework for community action in the field of marine environmental policy (Marine Strategy Framework Directive). http://data.europa.eu/eli/dir/2008/56/oj.
Fan, H.-R., Yang, K.-F., Hu, F.-F., Liu, S., Wang, K.-Y., 2016. The giant Bayan Obo REE-Nb-Fe deposit, China: controversy and ore genesis. Geosci. Front. 7 (3), 335–344. https://doi.org/10.1016/j.gsf.2015.11.005.
German, C.R., Masuzawa, T., Greaves, M.J., Elderfield, H., Edmond, J.M., 1995. Dissolved rare earth elements in the Southern Ocean: cerium oxidation and the influence of hydrography. Geochim. Cosmochim. Acta 59 (8), 1551–1558. https://doi.org/10.1016/0016-7037(95)00061-4.
Glasby, G.P., 1972. The mineralogy of manganese nodules from a range of marine environments. Mar. Geol. 13, 57–72.
Glasby, G.P., Stüben, D., Jeschke, G., Stoffers, P., Garbe-Schönberg, C.-D., 1997. A model for the formation of hydrothermal manganese crusts from the Pitcairn Island hotspot. Geochim. Cosmochim. Acta 61 (21), 4583–4597. https://doi.org/10.1016/s0016-7037(97)00262-7.
González, F.J., Somoza, L., Lunar, R., Martínez-Frías, J., Martín Rubí, J.A., Torres, T., Ortiz, J.E., Díaz del Río, V., Pinheiro, L.M., Magalhães, V.H., 2009. Hydrocarbon-derived ferromanganese nodules in carbonate-mud mounds from the Gulf of Cadiz: mud-breccia sediments and clasts as nucleation sites. Mar. Geol. 261 (1–4), 64–81. https://doi.org/10.1016/j.margeo.2008.11.005.
González, F.J., Somoza, L., Lunar, R., Martínez-Frías, J., Martin Rubí, J.A., Torres, T., Ortiz, J.E., Diaz-del-Rio, V., 2010. Internal features, mineralogy and geochemistry of ferromanganese nodules from the Gulf of Cadiz: the role of the Mediterranean Outflow Water undercurrent. J. Mar. Syst. 80 (3–4), 203–218.
González, F.J., Somoza, L., León, R., Medialdea, T., Torres, T., Ortiz, J.E., Lunar, R., Martínez-Frías, J., Merinero, R., 2012. Ferromanganese nodules and micro-hardgrounds associated with the Cadiz Contourite Channel (NE Atlantic): palaeoenvironmental records of fluid venting and bottom currents. Chem. Geol. 310-311, 56–78.
González, F.J., Somoza, L., Lunar, R., Martínez-Frías, J., Medialdea, T., León, R., Martín-Rubí, J.A., Torres, T., Ortiz, J.E., Marino, E., 2014. Polymetallic ferromanganese deposits research on the Atlantic Spanish continental margin. In: Hein, J.R., Barriga, F.J.A.S., Morgan, C.L. (Eds.), 43rd Underwater Mining Institute Conference (Lisbon).
González, F.J., Somoza, L., Hein, J.R., Medialdea, T., León, R., Urgorri, V., Reyes, J., Martín-Rubí, J.A., 2016. Phosphorites, Co-rich Mn nodules, and Fe-Mn crusts from Galicia Bank, NE Atlantic: reflections of Cenozoic tectonics and paleoceanography. Geochem. Geophys. Geosyst. 17, 346–374. https://doi.org/10.1002/2015GC005861.
González, F.J., Rincón-Tomás, B., Somoza, L., Santofimia, E., Medialdea, T., Madureira, P., López-Pamo, E., Hein, J.R., Marino, E., de Ignacio, C., Reyes, J., Hoppert, M., Reitner, J., 2020. Low-temperature, shallow-water hydrothermal vent mineralization following the recent submarine eruption of Tagoro volcano (El Hierro, Canary Islands). Mar. Geol. 430 https://doi.org/10.1016/j.margeo.2020.106333.
Gonzalez, F.J., Medialdea, T., Schillerup, H., Zananiri, I., Ferreira, P., Somoza, L., Monteys, X., Alcorn, T., Marino, E., Lobato, A.B., Zalba-Balda, I., Kuhn, T., Nyberg, J., Malyuk, B., Magalhães, V., Hein, J.R., Cherkashov, G., 2023. MINDeSEA – Exploring seabed mineral deposits in European Seas, metallogeny and geological potential for stategic and critical raw materials. In: The Green Stone Age: Exploration and Exploitation of Minerals for Green Technologies, 526. Geological Society of London Special Publication. https://doi.org/10.1144/SP526-2022-150.
Grousset, F.E., Biscaye, P.E., 2005. Tracing dust sources and transport patterns using Sr, Nd and Pb isotopes. Chem. Geol. 222, 149–167.
Grousset, F.E., Parra, M., Bory, A., Martinez, P., Bertrand, P., Shimmield, G., Ellam, R.M., 1998. Saharan wind regimes traced by the Sr-Nd isotopic composition of subtropical Atlantic sediments: last glacial maximumvs today. Quat. Sci. Rev. 17 (4–5), 395–409.
Halbach, P., Hebisch, U., Scherhag, C., 1981. Geochemical variations of ferromanganese nodules and crusts from different provinces of the Pacific Ocean and their genetic control. Chem. Geol. 34 (1), 3–17. https://doi.org/10.1016/0009-2541(81)90067-X.
Halbach, P., Friedrich, G., Von Stackelberg, U., 1988. The Manganese Nodule Belt of the Pacific Ocean. Geological Environment, Nodule Formation, and Mining Aspects x 254 pp. Stuttgart: Ferdinand Enke Verlag. ISBN 3 432 96381 5.
Haxel, G., Hedrick, J., Orris, J., 2002. In: Stauffer, Peter H., Hendley II, James W. (Eds.), Rare Earth Elements—Critical Resources for High Technology. United States Geological Survey. USGS Fact Sheet: 087–02.
Hedrick, J.B., Sinha, S.P., Kosynkin, V.D., 1997. Loparite, a rare-earth ore (Ce, Na, Sr, Ca)(Ti, Nb, Ta, Fe+3)O3, 250 (1–2), 0–470. https://doi.org/10.1016/s0925-8388(96)02824-1.
Hein, J.R., Koschinsky, A., 2014. Deep-ocean ferromanganese crusts and nodules. In: Turekian, H.D.H.K. (Ed.), Treatise on Geochemistry, second edition. Elsevier, Oxford, pp. 273–291.
Hein, J.R., Schwab, W.C., Davis, A., 1988. Cobalt- and platinum-rich ferromanganese crusts and associated substrate rocks from the Marshall Islands. Mar. Geol. 78 (3–4), 255–283. https://doi.org/10.1016/0025-3227(88)90113-2.

Hein, J.R., Bohrson, W.A., Schulz, M.S., Noble, M., Clague, D.A., 1992. Variations in the fine-scale composition of a Central Pacific ferromanganese crust: paleoceanographic implications. Paleoceanogrphy 7, 63–67. https://doi.org/10.1029/91PA02936.
Hein, J.R., Koschinsky, A., Halbach, P., Manheim, F.T., Bau, M., Kang, J.-K., Lubick, N., 1997. Iron and manganese oxide mineralization in the Pacific. In: Nicholson, K., Hein, J.R., Buhn, B., Dasgupta, S. (Eds.), Manganese Mineralization: Geochemistry and Mineralogy of Terrestrial and Marine Deposits, vol. 119. Special Publication Geological Society of London, London, pp. 123–138.
Hein, J.R., Koschinsky, A., Bau, M., Manheim, F.T., Kang, J.-K., Roberts, L., 2000. Co-rich ferromanganese crusts in the Pacific. In: Cronan, D.S. (Ed.), Handbook of Marine Mineral Deposits. CRC Marine Science Series. CRC Press, Boca Raton, Florida, pp. 239–279.
Hein, J.R., Koschinsky, A., McIntyre, B.R., 2005. Mercury- and silver-rich ferromanganese oxides, southern California Borderland: deposit model and environmental implications. Econ. Geol. 100, 1151–1168.
Hein, J.R., Schulz, M.S., Dunham, R.E., Stern, R.J., Bloomer, S.H., 2008. Diffuse flow hydrothermal manganese mineralization along the active Mariana and southern Izu-Bonin arc system, western Pacific. J. Geophys. Res. 113, B08S14. https://doi.org/10.1029/2007JB005432.
Hein, J.R., Conrad, T.A., Dunham, R.E., 2009. Seamount characteristics and mine-site model applied to exploration- and mining-lease-block selection for cobalt-rich ferromanganese crusts. Mar. Georesour. Geotechnol. 27 (2), 160–176. https://doi.org/10.1080/10641190902852485.
Hein, J.R., Mizell, K., Koschinsky, A., Conrad, T.A., 2013. Deep-ocean mineral deposits as a source of critical metals for high- and green-technology applications: comparison with land-based resources. Ore Geol. Rev. 51, 1–14. https://doi.org/10.1016/j.oregeorev.2012.12.001.
Hein, J.R., Spinardi, F., Okamoto, N., Mizell, K., Thorburn, D., Tawake, A., 2015. Critical metals in manganese nodules from the Cook Islands EEZ, abundances and distributions. Ore Geol. Rev. 68, 97–116. https://doi.org/10.1016/j.oregeorev.2014.12.011.
Hein, J.R., Conrad, T., Mizell, K., Banakar, V.K., Frey, F.A., Sager, W.W., 2016. Controls on ferromanganese crust composition and reconnaissance resource potential, Ninetyeast Ridge, Indian Ocean. Deep-Sea Res. I 110, 1–19. https://doi.org/10.1016/j.dsr.2015.11.006.
Holtstam, D., Andersson, U.B., Broman, C., Mansfeld, J., 2014. Origin of REE mineralization in the Bastnäs-type Fe-REE-(Cu-Mo-Bi-Au) deposits, Bergslagen, Sweden. Mineral. Deposita 49, 933–966. https://doi.org/10.1007/s00126-014-0553-0.
Ingram, B.L., Hein, J.R., Farmer, G.L., 1990. Age determinations and growth rates of Pacific ferromanganese deposits using strontium isotopes. Geochim. Cosmochim. Acta 54 (6), 1709–1721. https://doi.org/10.1016/0016-7037(90)90402-7.
Jackson, S., 2008. LAMTRACE data reduction software for LA-ICP-MS. In: Sylvester, P. (Ed.), Laser Ablation ICP-MS in the Earth Sciences: Current Practices and Outstanding Issues. Mineralogical Association of Canada Short Course Series; Mineralogical Association of Canada, Vancouver, BC, Canada, pp. 305–307.
Jochum, K.P., Nohl, U., Herwig, K., Lammel, E., Stoll, B., Hofmann, A.W., 2007. GeoReM: a new geochemical database for reference materials and isotopic standards. Geostand. Geoanal. Res. 29, 333–338. https://doi.org/10.1111/j.1751-908X.2005.tb00904.x.
Jochum, K.P., Weis, U., Stoll, B., Kuzmin, D., Yang, Q., Raczek, I., Jacob, D.E., Stracke, A., Birbaum, K., Frick, D.A., et al., 2011. Determination of reference values for NIST SRM 610-617 glasses following ISO guidelines. Geostand. Geoanal. Res. 35, 397–429. https://doi.org/10.1111/j.1751-908X.2011.00120.x.
Johnson, K.S., Coale, K.H., Berelson, W.M., Gordon, R.M., 1996. On the formation of the manganese maximum in the oxygen minimum, 60 (8), 0–1299. https://doi.org/10.1016/0016-7037(96)00005-1.
Josso, P., Pelleter, E., Pourret, O., Fouquet, Y., Etoubleau, J., Cheron, S., Bollinger, C., 2017. A new discrimination scheme for oceanic ferromanganese deposits using high field strength and rare earth elements. Ore Geol. Rev. 87, 3–15. https://doi.org/10.1016/j.oregeorev.2016.09.003.
Juteau, T., Bingöl, F., Noack, Y., Whitechurch, H., 1978. Preliminary results: mineralogy and geochemistry of alteration products in leg 45 basement samples. In: Initial Reports of the Deep Sea Drilling Project, 45, pp. 613–645. Washington.
Kandler, K., Schütz, L., Jäckel, S., Lieke, K., Emmel, C., Müller-Ebert, D., Ebert, M., Scheuvens, D., Schladitz, A., Šegvić, B., Wiedensohler, A., Weinbruch, S., 2011. Ground-based offline aerosol measurements at Praia, Cape Verde, during the Saharan Mineral Dust Experiment: microphysical properties and mineralogy. Tellus Ser. B 63 (4), 459–474.
Kfouri, L.O., Millo, C., de Lima, A.E., Silveira, C.S., Sant'Anna, L.G., Marino, E., González, F.J., Sayeg, I.J., Hein, J.R., Jovane, L., Bernardini, S., Lusty, P.A.J., Murton, B.J., 2021. Growth of ferromanganese crusts on bioturbated soft substrate, Tropic Seamount, northeast Atlantic Ocean. Deep Sea Res. Part I 175. https://doi.org/10.1016/j.dsr.2021.103586.
Klügel, A., Villinger, H., Römer, M., Kaul, N., Krastel, S., Lenz, K.-F., Wintersteller, P., 2020. Hydrothermal activity at a Cretaceous seamount, Canary Archipelago, caused by rejuvenated volcanism. Front. Mar. Sci. 7 https://doi.org/10.3389/fmars.2020.584571.
Koschinsky, A., Halbach, P., 1995. Sequential leaching of marine ferromanganese precipitates: genetic implications. Geochim. Cosmochim. Acta 59, 5113–5132.
Koschinsky, A., Halbach, P., Hein, J.R., Mangini, A., 1996. Ferromanganese crusts as indicators for paleoceanographic events in the NE Atlantic. Geol. Rundsch. 85 (3), 567–576. https://doi.org/10.1007/BF02369011.
Koschinsky, A., Stascheit, A., Bau, M., Halbach, P., 1997. Effects of phosphatization on the geochemical and mineralogical composition of marine ferromanganese crusts. Geochim. Cosmochim. Acta 61, 4079–4094. https://doi.org/10.1016/S0016-7037(97)00231-7.
Koschinsky, A., van Gerven, M., Halbach, P., 1995. First discovery and investigation of massive ferromanganese crusts in the NE Atlantic in comparison to hydrogenetic Pacific occurrences. Mar. Georesour. Geotechnol. 13, 375–391. https://doi.org/10.1080/10641199509388294.
Kuhn, T., Wegorzewski, A., Rühlemann, C., Vink, A., 2017. Composition, formation, and occurrence of polymetallic nodules. In: Sharma, R. (Ed.), Deep-Sea Mining: Resource Potential, Technical and Environmental Considerations. Springer International Publishing, Cham, Switzerland, pp. 23–63. ISBN 978-3-319-52557-0.
Lázaro, F.J., Gutiérrez, L., Barrón, V., Gelado, M.D., 2008. The speciation of iron in desert dust collected in Gran Canaria (Canary Islands): combined chemical, magnetic and optical analysis. Atmos. Environ. 42, 8987–8996. https://doi.org/10.1016/j.atmosenv.2008.09.035.
Lazarov, M., Horn, I., 2015. Matrix and energy effects during in-situ determination of Cu isotope ratios by ultraviolet-femtosecond laser ablation multicollector inductively coupled plasma mass spectrometry. Spectrochim. Acta Part B At. Spectrosc. 111, 64–73. https://doi.org/10.1016/j.sab.2015.06.013.
Long, K.R., Van Gosen, B.S., Foley, N.K., Cordier, Daniel, 2010. The principal rare earth elements deposits of the United States—A summary of domestic deposits and a global perspective. In: U.S. Geological Survey Scientific Investigations Report 2010–5220, 96 p. Available at. http://pubs.usgs.gov/sir/2010/5220/.
Lottermoser, B.G., 1990. Rare-earth element mineralisation within the Mt. Weld carbonatite laterite, Western Australia. Lithos 24 (2), 151–167. https://doi.org/10.1016/0024-4937(90)90022-s.
Machín, F., Hernández-Guerra, A., Pelegrí, J.L., 2006. Mass fluxes in the Canary Basin. Prog. Oceanogr. 70 (2–4), 416–447. https://doi.org/10.1016/j.pocean.2006.03.019.
Manceau, A., Gorshkov, A.I., Drits, V.A., 1992a. Structural chemistry of Mn, Fe, Co, and Ni in manganese hydrous oxides: part II. Information from EXAFS spectroscopy and electron and X-ray diffraction. Am. Mineral. 77, 1144–1157.
Manceau, A., Charlet, L., Boisset, M.C., Didier, B., Spadini, L., 1992b. Sorption and speciation of heavy metals on hydrous Fe and Mn oxides. From microscopic to macroscopic. Appl. Clay Sci. 7 (1–3), 201–223. https://doi.org/10.1016/0169-1317(92)90040-T.
Manceau, A., Drits, V.A., Silvester, E., Bartoli, C., Lanson, B., 1997. Structural mechanism of Co2+ oxidation by the phyllomanganate buserite. Am. Mineral. 82, 1150–1175.
Manheim, F.T., Lane-Bostwick, C.M., 1988. Cobalt in ferromanganese crusts as a monitor of hydrothermal discharge on the Pacific Sea floor. Nature 335 (6185), 59–62.
Marino, E., González, F.J., Somoza, L., Lunar, R., Ortega, L., Vázquez, J.T., Reyes, J., Bellido, E., 2017. Strategic and rare elements in Cretaceous-Cenozoic cobalt-rich ferromanganese crusts from seamounts in the Canary Island Seamount Province (northeastern tropical Atlantic). Ore Geol. Rev. https://doi.org/10.1016/j.oregeorev.2016.10.00.
Marino, E., González, F.J., Lunar, R., Reyes, J., Medialdea, T., Castillo-Carrión, M., Bellido, E., Somoza, L., 2018. High-resolution analysis of critical minerals and elements in Fe–Mn crusts from the Canary Island Seamount Province (Atlantic Ocean). Minerals 8 (7), 285. https://doi.org/10.3390/min8070285.
Marino, E., 2020. Costras de Ferromanganeso ricas en cobalto de los Montes Submarinos al Suroeste de las Islas Canarias. E-Prints Complutense. Tesis Doctoral, Universidad Complutense de Madrid. https://eprints.ucm.es/id/eprint/65857/.
Marino, E., González, F.J., Kuhn, T., Madureira, P., Wegorzewski, A.V., Mirao, J., Medialdea, T., Oeser, M., Miguel, C., Reyes, J., Somoza, L., Lunar, R., 2019. Hydrogenetic, diagenetic and hydrothermal processes forming ferromanganese crusts in the Canary Island Seamounts and their influence in the metal recovery rate with hydrometallurgical methods. Minerals 9 (7), 439. https://doi.org/10.3390/min9070439.
Maslennikov, V.V., Herrington, R.J., Ayupova, N.R., Danyushevsky, L.V., 2003. Implication of halmyrolysis in migration of REE during formation of ferruginous sedimentary rocks in Uzelga massive sulphide deposits, Southern Urals (Russia). In: Mineral Exploration and Sustainable Development (Eliopoulos, D. Ed.), Proceedings of the Seventh Biennial SGA Meeting on Mineral Exploration and Sustainable Development, Athens, pp. 147–150.
Medialdea, T., Somoza, L., González, F.J., Vázquez, J.T., de Ignacio, C., Sumino, H., Sánchez-Guillamón, O., Orihashi, Y., León, R., Palomino, D., 2017. Evidence of a modern deep water magmatic hydrothermal system in the Canary Basin (eastern Central Atlantic Ocean). Geochem. Geophys. Geosyst. 18 (8), 3138–3164. https://doi.org/10.1002/2017gc006889.
Mémery, L., Arhan, M., Alvarez-Salgado, X.A., Messias, M.-J., Mercier, H., Castro, C.G., Rios, A.F., 2000. The water masses along the western boundary of the south and equatorial Atlantic. Prog. Oceanogr. 47, 69–98. https://doi.org/10.1016/S0079-6611(00)00032-X.
Mendez, J., Guieu, C., Adkins, J., 2010. Atmospheric input of manganese and iron to the ocean: seawater dissolution experiments with Saharan and North American dusts. Mar. Chem. 120, 34–43. https://doi.org/10.1016/j.marchem.2008.08.006.
Milne, A., Landing, W., Bizimis, M., Morton, P., 2010. Determination of Mn, Fe, Co, Ni, Cu, Zn, Cd and Pb in seawater using high resolution magnetic sector inductively coupled mass spectrometry (HR-ICP-MS). Anal. Chim. Acta 665, 200–207. https://doi.org/10.1016/j.aca.2010.03.027.
Mohwinkel, D., Kleint, C., Koschinsky, A., 2014. Phase associations and potential selective extraction methods for selected high-tech metals from ferromanganese nodules and crusts with siderophores. Appl. Geochem. 43, 13–21. https://doi.org/10.1016/j.apgeochem.2014.01.010.
Muhs, D.R., Budahn, J., Skipp, G., Prospero, J.M., Patterson, D., BettisIii, E.A., 2010. Geochemical and mineralogical evidence for Sahara and Sahel dust additions to quaternary soils on Lanzarote, eastern Canary Islands, Spain. Terra Nova 22 (6), 399–410. https://doi.org/10.1111/j.1365-3121.2010.00949.x.

Muiños, S.B., Frank, M., Maden, C., Hein, J.R., van de Flierdt, T., Lebreiro, S.M., Gaspar, L., Monteiro, J.H., Halliday, A.N., 2008. New constraints on the Pb and Nd isotopic evolution of NE Atlantic water masses. Geochem. Geophys. Geosyst. 9 (2) https://doi.org/10.1029/2007gc001766 n/a–n/a.

Muiños, S.B., Hein, J.R., Frank, M., Monteiro, J.H., Gaspar, L., Conrad, T., Pereira, H.G., Abrantes, F., 2013. Deep-sea Fe–Mn crusts from the Northeast Atlantic Ocean: composition and resource considerations. Mar. Georesour. Geotechnol. 31 (1), 40–70. https://doi.org/10.1080/1064119X.2012.661215.

Neave, D.A., Shorttle, O., Oeser, M., Weyer, S., Kobayashi, K., 2018. Mantle-derived trace element variability in olivines and their melt inclusions. Earth Planet. Sci. Lett. 483, 90–104. https://doi.org/10.1016/j.epsl.2017.12.014.

Newman, H.R., 2011. The Mineral Industries of Morocco and Western Sahara U.S. Geological Survey Minerals Yearbook V. III, 10 pp.

Oeser, M., Weyer, S., Horn, I., Schuth, S., 2014. High-precision fe and mg isotope ratios of silicate reference glasses determined in situ by femtosecond LA-MC-ICP-MS and by solution nebulisation MC-ICP-MS. Geostand. Geoanal. Res. 38, 311–328. https://doi.org/10.1111/j.1751-908X.2014.00288.x.

Palomino, D., Vázquez, J.-T., Somoza, L., León, R., López-González, N., Medialdea, T., Fernández-Salas, L.-M., González, F.-J., Rengel, J.A., 2016. Geomorphological features in the southern Canary Island volcanic province: the importance of volcanic processes and massive slope instabilities associated with seamounts. Geomorphology 255, 125–139.

Pastor, M.V., Vélez-Belchí, P., Hernández-Guerra, A., 2015. Water masses in the Canary current large marine ecosystem. In: Valdés, L., Déniz-González, I. (Eds.), Oceanographic and Biological Features in the Canary Current Large Marine Ecosystem, IOCUNESCO, Paris. IOC Technical Series, vol. 115, pp. 73–79.

Pohl, C., Croot, P.L., Hennings, U., Daberkow, T., Budeus, G., Loeff, M., Rutgers, v.d., 2011. Synoptic transects on the distribution of trace elements (Hg, Pb, Cd, Cu, Ni, Zn, Co, Mn, Fe, and Al) in surface waters of the Northern- and Southern East Atlantic. J. Mar. Syst. 84 (1–2), 28–41. https://doi.org/10.1016/j. jmarsys.2010.08.003.

Post, J.E., 1999. Manganese oxide minerals: crystal structures and economic and environmental significance. Proc. Natl. Acad. Sci. U. S. A. 96, 3447–3545.

Rajani, R.P., Banakar, V.K., Parthiban, G., Mudholkar, A.V., Chodankar, A.R., 2005. Compositional variation and genesis of ferromanganese crusts of the Afanasiy–Nikitin Seamount, Equatorial Indian Ocean. J. Earth Syst. Sci. 114, 51–61. https://doi.org/10.1007/BF02702008.

Rona, P.A., 2003. Resources of the Sea floor. Science 299, 673–674. https://doi.org/10.1126/science.1080679.

Rudnick, R.L., Gao, S., 2014. Composition of the continental crust. In: Holland, H.D., Turekian, K.K. (Eds.), Treatise on Geochemistry, 2nd ed. Volume 4 : The Crust. Elsevier, Oxford, UK, pp. 1–51. ISBN : 978–0–08-098300-4.

Saager, P.M., de Baar, H.J.W., de Jong, J.T.M., Nolting, R.F., Schijf, J., 1997. Hydrography and local sources of dissolved trace metals Mn, Ni, Cu, and Cd in the Northeast Atlantic Ocean. Mar. Chem. 57, 195–216.

Sakellariadou, F., González, F.J., Hein, J.R., Rincón-Tomás, B., Arvanitidis, N., Kuhn, T., 2022. Seabed mining and blue growth: exploring the potential of marine mineral deposits as a sustainable source of rare earth elements (MaREEs) (IUPAC Technical Report). Pure Appl. Chem. 94 (3), 329–351. https://doi.org/10.1515/pac-2021-0325.

Santofimia, E., González, F.J., Rincón-Tomás, B., López-Pamo, E., Marino, E., Reyes, J., Bellido, E., 2022. The mobility of thorium, uranium and rare earth elements from Mid Ordovician black shales to acid waters and its removal by goethite and schwertmannite. Chemosphere 307 (Part 2), 135907. https://doi.org/10.1016/j.chemosphere.2022.135907.

Sarnthein, M., Thiede, J., Pflaumann, U., Erlenkeuser, H., Fiitterer, D., Koopmann, B., Lange, H., Seibold, E., 1982. Atmospheric and oceanic circulation patterns off Northwest Africa during the past 25 million years. In: von Rad, U., Hinz, K., Sarnthein, M., Seibold, E. (Eds.), Geology of Northwest Africa Continental Margin. Springer-Verlag, Berlin Heidelberg-New York, pp. 545–604.

Schijf, J., De Baar, H.J.W., Millero, F.J., 1995. Vertical distributions and speciation of dissolved rare earth elements in the anoxic brines of Bannock Basin, eastern Mediterranean Sea. Geochim. Cosmochim. Acta 59 (16), 3285–3299. https://doi.org/10.1016/0016-7037(95)00219-p.

Sholkovitz, E., Shaw, T., Schneider, D., 1992. The geochemistry of rare earth elements in the seasonally anoxic water column and porewaters of Chesapeake Bay. Geochim. Cosmochim. Acta 56 (9), 3389–3402. https://doi.org/10.1016/0016-7037(92)90386-w.

Somoza, L., Vázquez, J.T., Moya, A., Medialdea, T., Paredes, M., León, R., Fernández-Salas, L.M., González, F.J., Palomino, D., Equipo Científico-Técnico de la Ampliación de España al Oeste de las Islas Canarias, 2015. Presentación parcial de datos e información sobre los límites de la Plataforma Continental de España al oeste de las islas Canarias, conforme a la parte vi y el anexo ii de la convención de las naciones unidas sobre el derecho del mar. http://www.un.org/depts/los/clcs_new/submissions_files/esp77_14/esp_2014_es.pdf.

Somoza, L., González, F.J., Barker, S.J., Madureira, P., Medialdea, T., de Ignacio, C., Lourenço, N., León, R., Vázquez, J.T., Palomino, D., 2017. Evolution of submarine eruptive activity during the 2011-2012 El Hierro event as documented by hydroacoustic images and remotely operated vehicle observations. Geochem. Geophys. Geosyst. 18, 3109–3137.

Somoza, L., Rueda, J.L., Sánchez-Guillamón, O., Medialdea, T., Rincón-Tomás, B., González, F.J., Palomino, D., Madureira, P., López-Pamo, E., Fernández-Salas, L.M., Santofimia, E., León, R., Marino, E., Fernández-Puga, M.C., Vázquez, J.T., 2021. The interactive role of hydrocarbon seeps, hydrothermal vents and intermediate Antarctic/Mediterranean water masses on the distribution of some vulnerable deep-sea habitats in Mid Latitude NE Atlantic Ocean. Oceans 2 (2), 351–385. https://doi.org/10.3390/oceans2020021.

Taylor, S.R., McLennan, S.M., 1985. The Continental Crust; Its Composition and Evolution; an Examination of the Geochemical Record Preserved in Sedimentary Rocks. 312. Blackwell, Oxford.

The White House, 2021. Building resilient supply chains, revitalizing American manufacturing, and fostering broad-based growth. In: The White House Report. https://www.whitehouse.gov/wp-content/uploads/2021/06/100-day-supply-chain-review-report.pdf.

Usui, A., Nishi, K., Sato, H., Thornton, B., Kashiwabara, T., Tokumaru, A., Sakaguchi, A., Yamoaka, K., Kato, S., Nitahara, S., Suzuki, K., Ijima, K., Urabe, T., 2017. Continuous growth of hydrogenetic ferromanganese crusts since 17 Myr ago on Takuyo-Daigo Seamount, NW Pacific, at water depths from 800–5500 m. Ore Geol. Rev. 87, 71–87.

van den Bogaard, P., 2013. The origin of the Canary Island Seamount Province —new ages of old seamounts. Sci. Rep. 3, 2107. https://doi.org/10.1038/srep02107. http://www.nature.com/articles/srep02107#supplementary-information.

Varentsov, I.M., Drits, V.A., Gorshkov, A.I., Sivtsov, A.V., Sakharov, B.A., 1991. Mn-Fe oxyhydroxide crusts from Krylov Seamount (EasternAtlantic): mineralogy, geochemistry and genesis. Mar. Geol. 96 (1), 53–70. https://doi.org/10.1016/0025-3227(91)90201-E.

Vázquez, J.T., Somoza, L., Rengel, J.A., Medialdea, T., Millán, A., Alcalá, C., González, F. J., Jiménez, P., León, R., López-González, N., Palomino, D., López, F.J., García Muñoz, M., Martín, D., Sánchez-Guillamón, O., Correa, A., Martínez, J.C., Corbalán, A., Cruces, M., García, J.M., García, M., 2011. Informe científico-técnico de la campaña oceanográfica DRAGO0511. Ampliación de la plataforma continental de España al oeste de las islas Canarias, 273 pp.

Verplanck, P.L., Mariano, A.N., Mariano, A., 2016. Rare earth element ore geology of carbonatites. In: Verplanck, P., Hitzman, M. (Eds.), Rare Earth and Critical Elements in Ore Deposits. Society of Economic Geologists, Littleton, Colorado, pp. 5–32.

Wall, F., 2013. Rare earth elements. In: Critical Metals Handbook, pp. 312–339. https://doi.org/10.1002/9781118755341.ch13.

Wang, X.H., Peine, F., Schmidt, A., Schröder, H.C., Wiens, M., Schloßmacher, U., Müller, W.E.G., 2011. Concept of biogenic ferromanganese crust formation: coccoliths as bioseeds in crusts from Central Atlantic Ocean (Senghor seamount/Cape Verde). Nat. Prod. Commun. 6, 679–688.

Wegorzewski, A.V., Kuhn, T., 2014. The influence of suboxic diagenesis on the formation of manganese nodules in the Clarion Clipperton nodule belt of the Pacific Ocean. Mar. Geol. 357, 123–138. https://doi.org/10.1016/j.margeo.2014.07.004.

Wegorzewski, A.V., Kuhn, T., Dohrmann, R., Wirth, R., Grangeon, S., 2015. Mineralogical characterization of individual growth structures of Mn-nodules with different Ni+Cu content from the Central Pacific Ocean. Am. Mineral. 100, 2497–2508. https://doi.org/10.2138/am-2015-5122.

Yeo, I.A., Howarth, S.A., Spearman, J., Cooper, A., Crossouard, N., Taylor, J., Turnbull, M., Murton, B.J., 2019. Distribution of and hydrographic controls on ferromanganese crusts: Tropic Seamount, Atlantic. Ore Geol. Rev. 114, 103131. https://doi.org/10.1016/j.oregeorev.2019.103131.

Zawadzki, D., Maciąg, L., Blasco, I., González, F.J., Wernette, B., Marino, E., Kozub-Budzyń, G., Piestrzynski, A., Wróbel, R.J., 2021. Geochemistry and mineralogy of ferromanganese crusts from the Western Cocos-Nazca Spreading Centre, Pacific. Minerals 12 (5), 538. https://doi.org/10.3390/min12050538.

Zhong, Y., Chen, Z., Gonzalez, F.J., Zheng, X., Li, G., Luo, Y., Mo, A., Xu, A., Wang, S., 2018. Rare earth elements and yttrium in ferromanganese deposits from the South China Sea: distribution, composition and resource considerations. Acta Oceanol. Sin. 37 (7), 41–54. https://doi.org/10.1007/s13131-018-1205-5.

Zhou, B., Li, Z., Chen, C., 2017. Global potential of rare earth resources and rare earth demand from clean technologies. Minerals 7 (11), 203. https://doi.org/10.3390/min7110203.